



## “Boundary control of continuum robot for dynamic scanning task”

### Dual Program

Master in Optomechatronics from Centro de Investigaciones en Óptica, A.C. (CIO)  
International Master on Control and Robotics, Speciality: Control for Green Mechatronics from  
Université Bourgogne Franche-Comté and université Franche-Comté (UBFC)

#### *Internship conducted at:*

Femto - Sciences et Technologies

#### *Thesis presented by:*

Edgar Gabriel Ayala Pérez

#### *Advisor at CIO:*

*Dr. Gerardo Flores Colunga*

#### *Academic Tutor at UBFC:*

*Dr. Abdenbi Mohand-Ousaid*

#### *Internship supervisor:*

*Dr. Yongxin WU*

*Dr. Kanty RABENOROSOA*

*Pr. Yann LE GORREC*

**July 2021**

Besançon · Franche-Comté · France

## Special Thanks

To my parents, Rosy and Gabriel, to my sister Berenice and to my girlfriend Joselyne, for their unconditional support and love, for being with me since the beginning of my master. Without their motivation, even in the distance, I would not be where I am now.

To my university friends, Andrés, Gabriel, Juan Carlos, Octavio, René and Willie, for their true friendship and support among the years.

To my CIO, UBFC and Femto-st friends and colleagues, for the new experiences and companionship in the last two years.

To my friends Matthieu, Odile, Pascal, Patricia and Roland for helping me and being with me along my year in Besançon.

To Dr. Gerardo Flores (CIO), for accepting me in his work team and for the provided support in the double degree program. To my internship professors, Dr. Yongxin WU (Femto-st), Dr. Kanty RABENOROSOA (Femto-st) and Pr. Yann LE GORREC (Femto-st), for their help along the internship period.

To the *Consejo Nacional de Ciencia y Tecnología (CONACYT)* for the given economic support through the scholarship with CVU number 1004359 for National Master and Double Degree Program to perform my studies within the programs Master in Optomechatronics (CIO) and the International Master on Control and Robotics, Speciality: Control for Green Mechatronics (UBFC) in France.

To the Centro de Investigaciones en Óptica, A. C. (CIO), to the Université Bourgogne Franche-Comté (UBFC) and to the institute Franche-Comté Electronique Mécanique Thermique et Optique – Sciences et Technologies (Femto-st) for letting develop myself in an academic and professional way.



# Contents

<b>Abstract</b>	<b>4</b>
<b>Femto-st AS2M Department</b>	<b>5</b>
<b>Introduction</b>	<b>6</b>
<b>Nomenclature and notation</b>	<b>7</b>
<b>1 State of the Art</b>	<b>9</b>
1.1 Continuum Robots . . . . .	9
1.1.1 Structure . . . . .	9
1.1.2 Actuation . . . . .	10
1.1.3 Modeling . . . . .	10
1.2 Port Hamiltonian systems . . . . .	11
1.3 Contribution . . . . .	12
<b>2 Cosserat rod dynamics</b>	<b>14</b>
2.1 Rigid body transformation . . . . .	14
2.2 Balance equations . . . . .	15
2.3 Constitutive laws . . . . .	16
2.4 Dynamic PDE's . . . . .	16
2.5 Numerical simulation . . . . .	17
<b>3 Port Hamiltonian presentation</b>	<b>19</b>
3.1 Port Hamiltonian system of the optical fiber rod . . . . .	19
3.1.1 Port Hamiltonian model . . . . .	20
3.2 Port Hamiltonian system of the piezoelectric tube actuator . . . . .	23
3.2.1 Port Hamiltonian model . . . . .	24
3.3 Interconnected model . . . . .	24
<b>4 Rod's numerical resolution and validation</b>	<b>26</b>
4.1 Spatial discretization . . . . .	26
4.1.1 Interconnected model . . . . .	28
4.2 Numerical validation . . . . .	29
<b>5 Experimental setup and parameters identification</b>	<b>31</b>
5.1 Equipment . . . . .	31
5.2 CAD model . . . . .	31
5.3 Experimental setup . . . . .	32
5.4 Optical fiber parameters identification . . . . .	33
5.5 Piezoelectric tube parameters identification . . . . .	38

<b>6</b>	<b>Controller</b>	<b>39</b>
6.1	IDA-PBC Boundary Controller . . . . .	39
6.2	Simulation . . . . .	41
6.3	Experimental validation . . . . .	44
<b>7</b>	<b>Conclusions and Perspectives</b>	<b>47</b>
	<b>Bibliography</b>	<b>48</b>

---

# Boundary control of continuum robot for dynamic scanning task

Edgar Gabriel Ayala Pérez  
FEMTO-ST, AS2M Department  
26 rue de l'Épitaphe, 25000, Besançon, France  
[edgar.ayaperez@femto-st.fr](mailto:edgar.ayaperez@femto-st.fr)

---

## Abstract

The usage of continuum robot techniques is becoming more and more popular in medical applications, specially for minimally invasive surgical procedures. Some of these procedures may include, for example, brain, cardiac, and vascular surgeries, optical coherence tomography (OCT), among others.

This work presents a port Hamiltonian system (PHS) approach for a 5cm long optical fiber continuum robot actuated by a 3cm long *PT230.94* piezoelectric tube. The purpose of the robot is to effectuate micro-scanning tasks. A non-linear infinite dimensional PHS model of the 3D continuum robot was obtained from the Cosserat rod dynamical equations also shown in this work. A comparison of the rod's behavior of the rod was made using the two different models, obtaining a similar response. Also, physical parameters of the optical fiber robot and the piezoelectric tube actuator were identified with an experimental setup in the AS2M department at Femto-st institute. Then an energy-based interconnection damping assignment passivity based control (IDA-PBC) is synthesised as a boundary controller to control a desired scanning trajectory of the robot's free end. The controller is first simulated by giving an  $[x, y]$  desired position and then a desired 2D spiral scanning trajectory. The experimental part was then validated in the  $x$  direction with a desired end point and with a desired trajectory.

**Key Words:** Continuum Robot, port Hamiltonian system, scanning, optical fiber, boundary control.

## Femto-st AS2M department



The Femto-st Institute "Franche-Comté Electronique Mécanique Thermique et Optique-Sciences et Technologies", is a joint research institution, which is under the quadruple authority of the Université de Franche-Comté (UFC), the Centre National de la Recherche Scientifique (CNRS), the Ecole Nationale Supérieure de Mécanique et Microtechniques (EN-SMM) and the Université de la Technologie Belfort-Montbéliard (UTBM).

The Automatique et Systèmes Micro-Mécatroniques (AS2M) department is focused in the research disciplines of robotics, mechatronics, automatic control and artificial intelligence. The department has acquired international recognition and experience in the design and control of micro and nano positioning and assembly systems, and micro robotics for minimally invasive surgery.

## Introduction

The medical applications for continuum robots have been growing in the last years. The main purpose of using these robots is to perform minimally invasive surgeries to reduce the potential risks and to improve the success of the involved procedures in surgeries [1]. Some examples of the most important surgeries and the problems solved with continuum robots are:

- Neurosurgical: Wide cranium openings, tissue pushed aside to gain access to deeper regions of the brain, proximity to structures with important functionalities.
- Otolaryngology: Usually performed with straight or flexible endoscopes and other instruments entering to the nostrils, mouth or ears. These instruments have a lack of dexterity, such that some regions remain inaccessible.
- Cardiac Surgery: Most of the the heart procedures require open cardiac surgery. Catheter based operations are enabling minimally invasive surgeries, however, some difficulties are found such as a limited ability to apply and control forces necessary for performing the surgery and the challenge of positioning the catheter within a beating heart.
- Vascular Surgery: These procedures often include the use of catheters and guidewires to perform injections, drain fluids and insert additional surgical instruments. The main challenges are similar to the cardiac surgeries.

The main motivation for this project is to develop a new reliable PHS non-linear model for a continuum robot and to control its position with a control law also based in a PHS approach. In this work, numerical simulations and a experimental validation of a continuum robot for micro-scanning tasks will be presented. The distribution of the work is the following: first, the notation used for the rod; second, the state of the art and the contribution of this project in Section 1; third, the dynamic equations for the Cosserat rod model in Section 2; fourth, the port Hamiltonian models for the rod and the actuator in Section 3; fifth, the rod's port Hamiltonian model validation in Section 4; sixth, the presentation of the experimental setup and the physical parameters identification of the optical fiber and the piezoelectric tube in Section 5; finally, in Section 7, the controller is presented with numerical simulations and the experimental validation.

## Nomenclature and notation

The nomenclature used in this work for the rods is shown in Table 1 and Table 2 according to [2] and [3]. Also the partial derivative  $\frac{\partial}{\partial s}$  will be denoted using the subindex  $s$  and the partial derivative  $\frac{\partial}{\partial t}$  will be denoted using the subindex  $t$ . For example:

$$\frac{\partial \mathbf{p}}{\partial s} = \mathbf{p}_s, \quad \frac{\partial \mathbf{p}}{\partial t} = \mathbf{p}_t$$

**Table 1:** Rod's nomenclature

Value	Units	Definition
$s$	m	Reference arclength
$t$	s	Time
$\mathbf{p}$	m	Global position in Cartesian coordinates
$\mathbf{R}$	-	Rotation matrix of material orientation; Express internal loads un the global frame
$\mathbf{n}$	N	Internal force in the global frame
$\mathbf{m}$	Nm	Internal moment in the global frame
$\mathbf{f}$	N/m	Distributed force in the global frame
$\mathbf{l}$	Nm/m	Distributed moment in the global frame
$\mathbf{v}$	-	Rate of change of position with respect to arclength in the local frame
$\mathbf{v}^*$	-	Value of $\mathbf{v}$ when $\mathbf{n} = \mathbf{v}_t = 0$
$\mathbf{u}$	1/m	Curvature vector in the local frame
$\mathbf{u}^*$	1/m	Value of $\mathbf{u}$ when $\mathbf{m} = \mathbf{u}_t = 0$
$\mathbf{q}$	m/s	Velocity in the local frame
$\boldsymbol{\omega}$	1/s	Angular velocity in the local frame
$A$	m <sup>2</sup>	Cross-sectional area
$\rho$	kg/m <sup>3</sup>	Material density



**Table 2:** Rod's nomenclature

Value	Units	Definition
$\mathbf{J}$	$\text{m}^4$	Second mass moment of inertia tensor $\mathbf{J} = \begin{bmatrix} I_{xx} & 0 & 0 \\ 0 & I_{yy} & 0 \\ 0 & 0 & I_{zz} \end{bmatrix}$
$\mathbf{K}_{se}$	N	Stiffness matrix for shear and extension $\mathbf{K}_{se} = \begin{bmatrix} GA & 0 & 0 \\ 0 & GA & 0 \\ 0 & 0 & EA \end{bmatrix}$
$\mathbf{K}_{bt}$	$\text{Nm}^2$	Stiffness matrix for bending and torsion $\mathbf{K}_{bt} = \begin{bmatrix} EI_{xx} & 0 & 0 \\ 0 & EI_{yy} & 0 \\ 0 & 0 & GI_{zz} \end{bmatrix}$
$\mathbf{B}_{se}$	N s	Damping matrix for shear and extension
$\mathbf{B}_{bt}$	$\text{Nm}^2\text{s}$	Damping matrix for bending and torsion
$E$	Pa	Young's modulus
$G$	Pa	Shear's modulus
$\mathbf{I}$	$\text{m}^4$	Cross-sectional area moment of inertia
$\mathbf{C}$	$\text{kg/n}^2$	Square law drag coefficient matrix
$\mathbf{g}$	$\text{m/s}^2$	Gravitational acceleration vector
$(\cdot)$	-	Mapping from $\mathbb{R}^3$ to $\mathfrak{se}(3)$ $(\hat{\mathbf{u}}) = \begin{bmatrix} 0 & -u_3 & u_2 \\ u_3 & 0 & -u_1 \\ -u_2 & u_1 & 0 \end{bmatrix}$
$(\cdot)^\vee$	-	Mapping from $\mathfrak{se}(3)$ to $\mathbb{R}^3$ $(\hat{\mathbf{u}})^\vee = \mathbf{u}$

# 1 State of the Art

## 1.1 Continuum Robots

Robots can be classified in two branches, discrete and continuous [1]. When the number of joints approaches to infinity and the links' length approaches to zero, the robot is considered as a continuum robot. In general, the shape and the structure of these continuum robots could be defined and elastic member of infinite degrees of freedom. Thanks to this properties, continuum robots can be constructed at smaller scales in comparison to those with discrete joints.

Figure 1 shows that the continuum robots could be internally classified by their structure and the actuation mode.

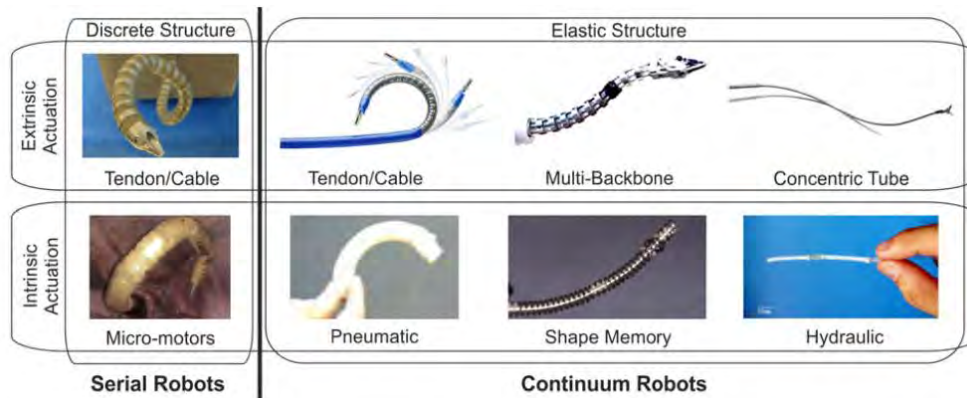


Figure 1: Robots classification by structure and actuation

### 1.1.1 Structure

For the structure classification, the following types could be found in [1]:

- Single back-bone: They have one central elastic structure that supports the passage of the actuator or transmission elements.
- Multi-backbone: They are composed by multiple parallel elastic elements constrained to each other.
- Concentric-tube: These robots are usually composed by multiple precurved elastic tubes that are inserted inside of each other.

There are two important principles to take into account when talking in the structural design of the robots, the workspace and their stiffness. Both characteristics should be large enough so the robot could do the required tasks.

### 1.1.2 Actuation

In actuation terms, there can be found two main classifications in [1] according to where the actuation occurs:

- Intrinsic: When the actuator is found within the moving structure.
- Extrinsic: When the actuator is found outside the main moving structure and the movement is transmitted through mechanical parts.

For *intrinsic* actuators, hydraulic and pneumatic chambers are being developed along with a shape memory effect of some materials, embedded micromotors and others. On the other hand, tendon/cable and multiback-bone structures are used as *extrinsic* actuators among others.

### 1.1.3 Modeling

Figure 2 presents some of the basic categories for describing most of the continuum robots models [1]. The main two categories could be separated in *Kinematics Frameworks* and *Mechanics Frameworks* both internally separated in discrete and continuous approaches.

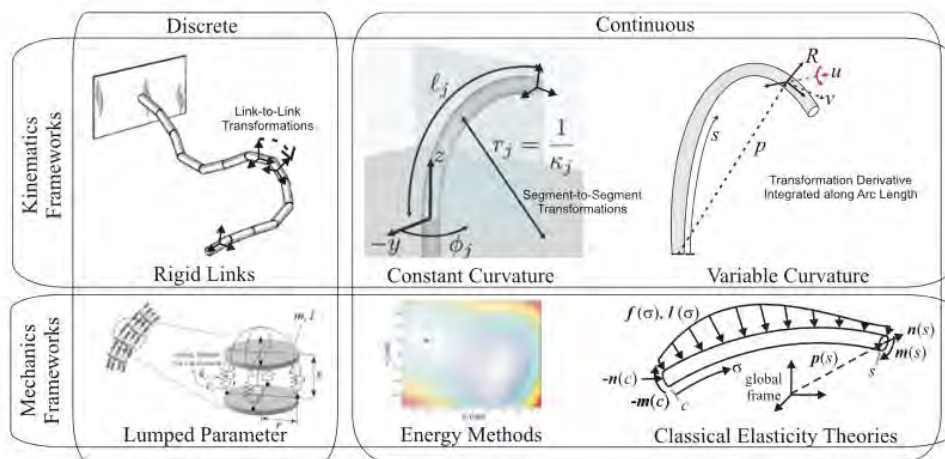


**Figure 2:** Continuum robots modeling methods

The continuous approach in the *Kinematics Frameworks* could be separated in:

- Constant-curvature: Represents the continuum robot geometry with a finite number of mutually tangent curved segments each one having a constant curvature along its length.
- Variable-curvature: Describe a continuously evolving reference frame along the length of the robot.

Also, the continuous approach for the *Mechanics Frameworks*, in which this work is based, could be classified in:

- Energy methods: Can be used to determine the shape of continuum robots using either lumped or distributed parameter descriptions
- Classical elasticity theories: Some of these theories for long slender objects such as rods and strings have been applied to continuum robots. Cosserat rod theory and Kirchhoff rod theory have become popular methods to model these robots.

## 1.2 Port Hamiltonian systems

Port-based modeling of physical systems is based on viewing the system as the interconnection of three types of ideal elements: dynamical energy-storing elements, static energy-dissipating elements, and static lossless energy-routing elements. The essence of port-based modeling and port-Hamiltonian systems is represented in Figure 3. The energy-storing elements  $S$  and the energy-dissipating elements  $R$  are linked to a central energy-routing structure, geometrically defined as a Dirac structure. This linking takes place in pairs forms  $(f, e)$  of equally dimensioned vectors usually known as flow and effort variables [4].

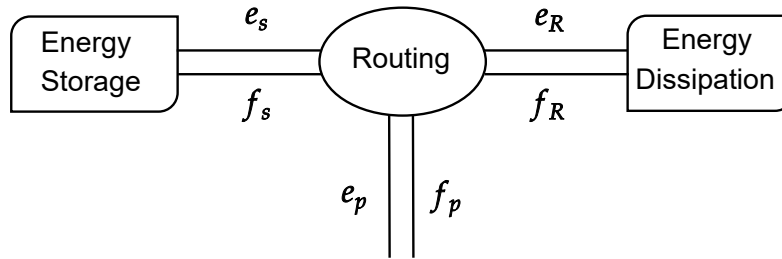


**Figure 3:** From port-based modeling to a port-Hamiltonian system

The basic and most important property of a Dirac structure is the power conservation. The Dirac structure links the flow and effort variables  $f = (f_S, f_R, f_P)$  and  $e = (e_S, e_R, e_P)$  in such a way that the total power  $e^T f = 0$ . The integration of the flow variable  $f_S$  for energy storage, leads to an equally dimensioned vector of state variables  $x$  satisfying  $\dot{x} = -f_S$ . Thus, the energy storage is expressed by the Hamiltonian  $\mathcal{H}$ , defining the effort variables vector as  $e_S = \nabla \mathcal{H}(x)$  where  $\nabla \mathcal{H}(x)$  is the column vector of the partial derivatives of  $\mathcal{H}$ . Also, the energy dissipation is any relation  $R$  between the flow and effort variables  $f_R$  and  $e_R$  of the energy dissipation port such that  $e_R^T f_R \leq 0$ .

An input-state-output port Hamiltonian system is finally expressed as in equation (1) where  $J = J^T$  and  $R = R^T \geq 0$ ,  $u = e_p$  is the input vector and  $y = f_p$  is the output vector [4].

$$\begin{aligned}\dot{x} &= (J - R)\nabla\mathcal{H}(x) + gu \\ y &= g^T\nabla\mathcal{H}(x)\end{aligned}\quad (1)$$

Energy based modeling can provide a modular presentation for interconnected systems, secondly, they provide different passivity based control methods which have clear physical interpretation.

### 1.3 Contribution

The main objective of this project was to develop a scanning continuum robot with an actuation at the boundary (base). This continuum robot consisted in an optical fiber rod and a piezoelectric tube actuator. This optical fiber continuum robot exhibits large deformations and highly nonlinear behaviors that will be described using Cosserat rods [2], [3], [5]. In order to deal with the multi physical nature of this system and the interconnection between between the continuum robot and the actuator, the port Hamiltonian framework was be investigated and derived. The port Hamiltonian formulations are indeed particularly well adapted for the modeling and control of nonlinear multi-physical systems [6], [7]. First, a suitable PHS mathematical model of the piezoelectric tube actuated continuum robot was derived and validated with numerical simulations. Then, the next step was to design a boundary control law for achieving efficient and accurate dynamic scanning tasks. As mention in Section 1.2, this kind of model is based on the principle of energy conservation and exhibits the systems properties and provides a clear physical interpretation of control design strategies. Both, the proposed PHS model and control law, were performed and validated numerically and experimentally.

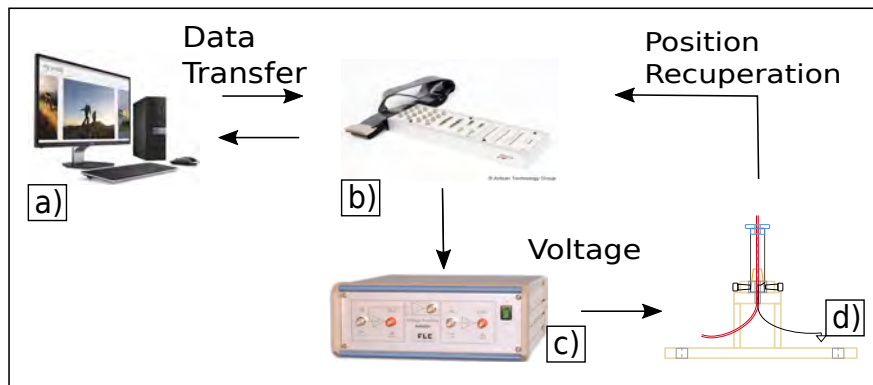


**Figure 4:** a) Simulink/ControlDesk interface; b) Dspace controller board; c) 20X Voltage amplifier; d) Optical fiber continuum robot

Figure 4 shows in a general way the project setup. An interface via *Simulink* and *ControlDesk* will communicate a dSpace controller board in order to send the control signal and receive the position information (Figure 4a, 4b). The dSpace board will send the necessary voltage to the *FLC A400DI* voltage amplifier in order to move the piezoelectric tube actuator in the  $x$  direction (Figure 4c, 4d). Finally, the tip's position of the optical fiber continuum robot and the piezoelectric tube will be recuperated with two Keyence sensors respectively, to implement the control law.

## 2 Cosserat rod dynamics

In this section a general and simple derivation of the dynamic partial differential equations is presented. This PDE's are a combination of the partial derivatives in space  $s$  and time  $t$ .

### 2.1 Rigid body transformation

In Cosserat-rod theory, a slender rod can be approximated as a one-dimensional object. The rod is characterized by its centerline curve  $\mathbf{p}(s, t) \in \mathbb{R}^3$  and its material orientation  $\mathbf{R}(s, t) \in SO(3)$  as functions of the arclength that will vary from zero at its base to the rod's length  $L$  ( $s \in [0, L]$ ) and the time  $t$  as shown in Figure 5. Hence, a rigid body transformation of the rod could be expressed as in equation (2). [5]

$$\mathbf{g}(s, t) = \begin{bmatrix} \mathbf{R}(s, t) & \mathbf{p}(s, t) \\ 0 & 1 \end{bmatrix} \quad (2)$$

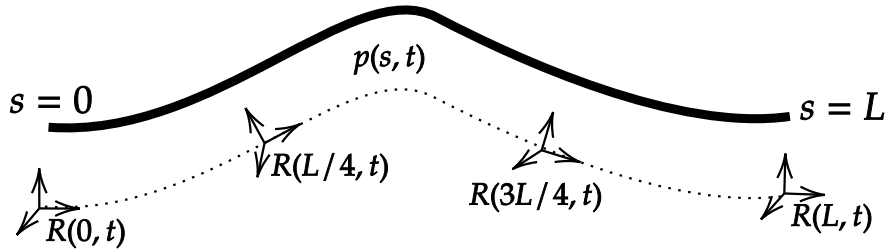


**Figure 5:** Representation of the rod as a one-dimensional object with arclength  $s \in [0, L]$

The kinematic variable in the local frame,  $\mathbf{v}(s, t)$ , is introduced to represent the linear rate of change of the rigid body transformation (first derivative of the position) with respect to  $s$ . Also, the variable in the local frame,  $\mathbf{u}(s, t)$ , is introduced to represent the angular rate of change (curvature) of the rigid body transformation with respect to  $s$ . The variables presented before can be expressed as in equations (3) and (4) respectively.

$$\mathbf{v} = \mathbf{R}^T \mathbf{p}_s \quad (3)$$

$$\mathbf{u} = (\mathbf{R}^T \mathbf{R}_s)^\vee \quad (4)$$

Analogous to these expressions, the linear velocity and the angular velocity at the local frame could be expressed as in equations (5) and (6) respectively.

$$\mathbf{q} = \mathbf{R}^T \mathbf{p}_t \quad (5)$$

$$\boldsymbol{\omega} = (\mathbf{R}^T \mathbf{R}_t)^\vee \quad (6)$$

## 2.2 Balance equations

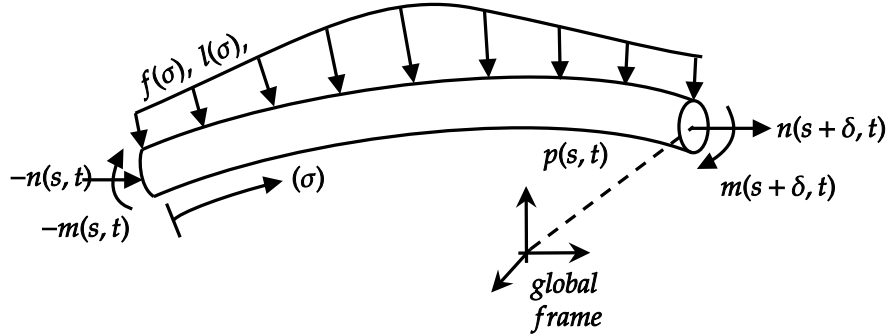


**Figure 6:** Infinitesimal section of the rod from  $s$  to  $s + \delta$  subjected to distributed forces  $\mathbf{f}$  and distributed momentums  $\mathbf{l}$ . Internal forces  $\mathbf{n}$  and  $\mathbf{m}$  are expressed in the global frame

Figure 6 shows the internal forces and momentum so as the distributed forces and momentum along the rod. The internal force in the rod is expressed by  $\mathbf{n}(s, t)$  and the sign convention is chosen to represent this forces as the force that the material at  $s + \delta$  exerts at  $s - \delta$ . This convention is used also in the internal momentum expressed by  $\mathbf{m}(s, t)$ . The distributed forces and distributed momentum along the rod are expressed as  $\mathbf{f}(\sigma)$  and  $\mathbf{l}(\sigma)$  respectively. Equation (7) gives the expression of the dynamic balance equation for the forces. Likewise, equation (8) represents the expression of the dynamic balance equation for the momentum.

$$\mathbf{n}(s + \delta) - \mathbf{n}(s) + \int_s^{s+\delta} \mathbf{f}(\sigma) d\sigma = \int_s^{s+\delta} \rho A \mathbf{p}_{tt} d\sigma \quad (7)$$

$$\begin{aligned} & \mathbf{m}(s + \delta) - \mathbf{m}(s) + \mathbf{p}(s + \delta) \times \mathbf{n}(s + \delta) + \mathbf{p}(s) \times \mathbf{n}(s) \\ & + \int_s^{s+\delta} [\mathbf{l}(\sigma) + \mathbf{p}(\sigma) \times \mathbf{f}(\sigma) d\sigma] = \int_s^{s+\delta} \frac{\partial}{\partial t} (\rho A \mathbf{p} \times \mathbf{p}_t + \mathbf{R} \rho \mathbf{J} \boldsymbol{\omega}) d\sigma \end{aligned} \quad (8)$$

By applying the derivative with respect to  $s$ , and applying the proper substitutions, the classical form differential equations are obtained as shown in (9) and (10).

$$\mathbf{n}_s + \mathbf{f} = \rho A \mathbf{p}_{tt} = \rho A \mathbf{R} (\hat{\boldsymbol{\omega}} \mathbf{q} + \mathbf{q}_t) \quad (9)$$

$$\mathbf{m}_s + \mathbf{l} + \mathbf{p}_s \times \mathbf{n} = \rho \mathbf{J} \mathbf{R}_{tt} = \rho \mathbf{R} (\hat{\boldsymbol{\omega}} \mathbf{J} \boldsymbol{\omega} + \mathbf{J} \boldsymbol{\omega}_t) \quad (10)$$



## 2.3 Constitutive laws

The difference between the kinetic variables in the local frame  $\mathbf{v}$  and  $\mathbf{u}$  in the rod's initial state and in the deformed state  $\mathbf{v}^*$  and  $\mathbf{u}^*$  are related to various mechanical modes of strain. [5]

The difference of the transverse shear in  $x$  and  $y$  directions correspond to  $\mathbf{v}_x - \mathbf{v}_x^*$  and  $\mathbf{v}_y - \mathbf{v}_y^*$  while the axial elongation or stretch in  $z$  direction corresponds to  $\mathbf{v}_z - \mathbf{v}_z^*$ . In a similar way, the difference of the bending in  $x$  and  $y$  directions correspond to  $\mathbf{u}_x - \mathbf{u}_x^*$  and  $\mathbf{u}_y - \mathbf{u}_y^*$  while the torsion around  $z$  axis corresponds to  $\mathbf{u}_z - \mathbf{u}_z^*$ .

Using the relations above, the constitutive laws shown in equation (11) and equation (12) relating these variables with the internal forces and momentum can be found.

$$\mathbf{n} = \mathbf{R}\mathbf{K}_{se}(\mathbf{v} - \mathbf{v}^*) \quad (11)$$

$$\mathbf{m} = \mathbf{R}\mathbf{K}_{bt}(\mathbf{u} - \mathbf{u}^*) \quad (12)$$

$$\mathbf{v} = \mathbf{R}^T \mathbf{K}_{se}^{-1} \mathbf{n} + \mathbf{v}^* \quad (13)$$

$$\mathbf{u} = \mathbf{R}^T \mathbf{K}_{bt}^{-1} \mathbf{m} + \mathbf{u}^* \quad (14)$$

## 2.4 Dynamic PDE's

The first dynamic PDE's for the Cosserat rod could be found by solving equations (3), (4), (9) and (10) for  $\mathbf{p}_s$ ,  $\mathbf{R}_s$ ,  $\mathbf{n}_s$  and  $\mathbf{m}_s$  respectively. Then, the derivative with respect to  $s$  of equation (5) could be obtained by making the proper substitutions as shown in equation (15). And finally, to obtain the last differential equation, the derivative of equation (6) with respect to  $s$  should be performed. By taking  $(-\hat{\mathbf{u}}\hat{\boldsymbol{\omega}} + \hat{\mathbf{u}}\hat{\boldsymbol{\omega}})^\vee = -\hat{\mathbf{u}}\boldsymbol{\omega}$ , equation (16) is found.

$$\begin{aligned} \mathbf{q}_s &= \mathbf{R}_s^T \mathbf{p}_t + \mathbf{R}^T \mathbf{p}_{ts} \\ \mathbf{q}_s &= (\mathbf{R}\hat{\mathbf{u}})^T \mathbf{R}\mathbf{q} + \mathbf{R}^T (\mathbf{R}\hat{\boldsymbol{\omega}}\mathbf{v} + \mathbf{R}\mathbf{v}_t) \\ \mathbf{q}_s &= \mathbf{v}_t - \hat{\mathbf{u}}\mathbf{q} + \hat{\boldsymbol{\omega}}\mathbf{v} \end{aligned} \quad (15)$$

$$\begin{aligned} \hat{\boldsymbol{\omega}}_s &= \mathbf{R}_s^T \mathbf{R}_t + \mathbf{R}^T \mathbf{R}_{ts} \\ \hat{\boldsymbol{\omega}}_s &= (\mathbf{R}\hat{\mathbf{u}})^T \mathbf{R}\hat{\boldsymbol{\omega}} + \mathbf{R}^T (\mathbf{R}\hat{\boldsymbol{\omega}}\hat{\mathbf{u}} + \mathbf{R}\mathbf{u}_t) \\ \boldsymbol{\omega}_s &= \mathbf{u}_t - \hat{\mathbf{u}}\boldsymbol{\omega} \end{aligned} \quad (16)$$

Finally the set of the dynamic PDE's for the Cosserat rod are shown in equation (17).

$$\begin{aligned}
 \mathbf{p}_s &= \mathbf{R}\mathbf{v} \\
 \mathbf{R}_s &= \mathbf{R}\hat{\mathbf{u}} \\
 \mathbf{n}_s &= \rho A \mathbf{R}(\hat{\boldsymbol{\omega}}\mathbf{q} + \mathbf{q}_t) - \mathbf{f} \\
 \mathbf{m}_s &= \rho \mathbf{R}(\hat{\boldsymbol{\omega}}\mathbf{J}\boldsymbol{\omega} + \mathbf{J}\boldsymbol{\omega}_t) - \hat{\mathbf{p}}_s \mathbf{n} - \mathbf{l} \\
 \mathbf{q}_s &= \mathbf{v}_t - \hat{\mathbf{u}}\mathbf{q} + \hat{\boldsymbol{\omega}}\mathbf{v} \\
 \boldsymbol{\omega}_s &= \boldsymbol{\omega}_t - \hat{\mathbf{u}}\boldsymbol{\omega}
 \end{aligned} \tag{17}$$

## 2.5 Numerical simulation

As an example, the code in [8] was taken. The dynamics of a cantilever rod with the parameters shown in table 3 were simulated. A force of  $[0.5 \ 0 \ 0]N$  at the tip was considered as an initial state of the rod, then, the force was released. Figure 7 shows the first few frames of the simulation. Figure 8 shows the tip's position in time. A very small damping was considered to perform the simulation.

**Table 3:** Main rod's parameters

Parameter	Value	Units
Length (L)	0,4	m
Young 's modulus (E)	207	GPa
Radius (r)	0,0012	m
Density ( $\rho$ )	8000	kg/m <sup>3</sup>

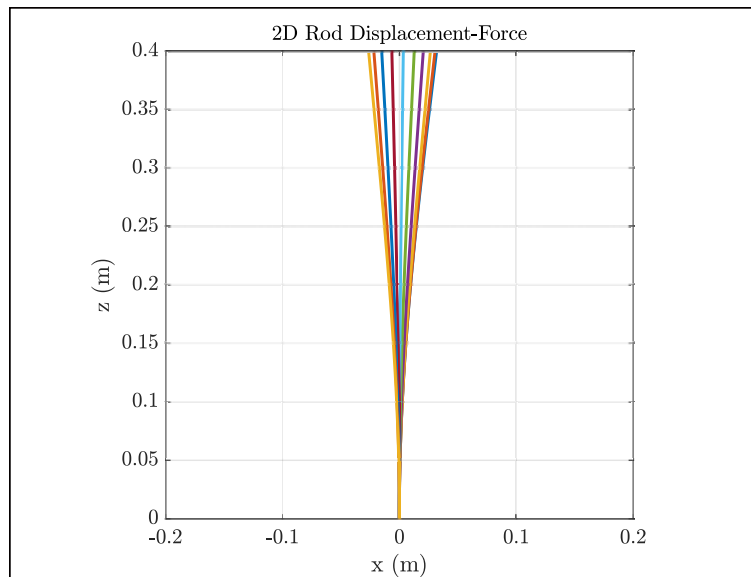


**Figure 7:** A force of 0.5 N is applied to the rod's tip and then released

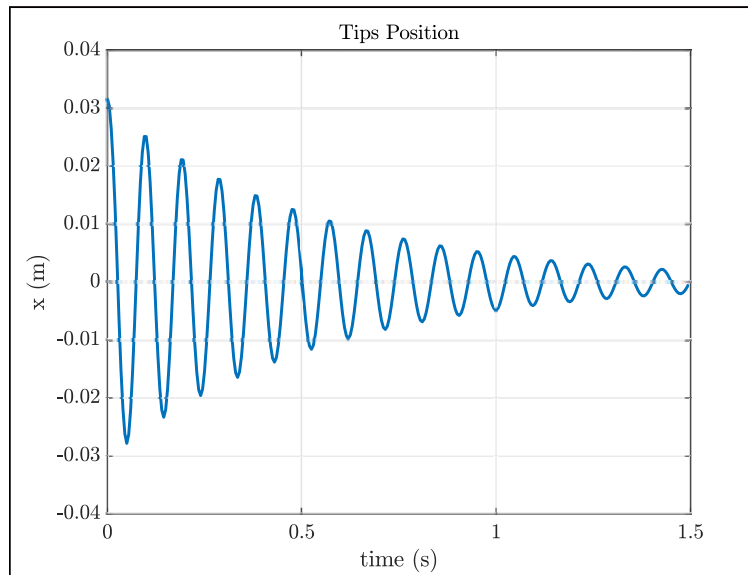


**Figure 8:** Tip's position with very small damping

### 3 Port Hamiltonian presentation

The main purpose of this section is to derive a proper Hamiltonian model of rod and the actuator. This is achieved by choosing the proper energy variables (state variables) and co-energy variables for the system. Also, the expression for total energy (Hamiltonian) of the rod is presented in this section.

#### 3.1 Port Hamiltonian system of the optical fiber rod

The first energy variable can be choose as the difference of the shear and axial elongation of the deformed state and original state as in equation (18). The second state variable is related to the internal translational momentum of the rod as in equation (19).

$$\mathbf{x}_1 = \mathbf{v} - \mathbf{v}^* \quad (18)$$

$$\mathbf{x}_2 = \rho A \mathbf{p}_t = \rho A \mathbf{q} \quad (19)$$

The third state variable is related to the difference in bending and torsion (curvature) of the deformed state and the original state of the rod as in equation (20). Then, the fourth energy variable is related to the internal rotational momentum of the rod. Equation (21) shows this state variable.

$$\mathbf{x}_3 = \mathbf{u} - \mathbf{u}^* \quad (20)$$

$$\mathbf{x}_4 = \rho \mathbf{J} \mathbf{R}_t = \rho \mathbf{J} \boldsymbol{\omega} \quad (21)$$

The total mechanical energy can be expressed by the sum of the potential elastic energy and the kinetic energy of the rod and integrating for each infinitesimal part for  $s \in [0 L]$ .

The potential elastic energy relates the first energy variable (equation (18)) with the first co-energy variable (equation(25)) and the third energy variable (equation (20)) with the third co-energy variable (equation(27)). Equation (22) gives the total potential energy of the system which includes the shear and curvature of the rod.

$$\begin{aligned} \mathcal{V} &= \frac{1}{2} \int_0^L [\mathbf{K}_{se} \mathbf{x}_1^2 + \mathbf{K}_{bt} \mathbf{x}_3^2] ds \\ &= \frac{1}{2} \int_0^L [(\mathbf{K}_{se} (\mathbf{v} - \mathbf{v}^*))^2 + \mathbf{K}_{bt} (\mathbf{u} - \mathbf{u}^*)^2] ds \end{aligned} \quad (22)$$

The kinetic energy relates the second energy variable (equation (19)) with the second co-energy variable (equation(26)) and the fourth energy variable (equation (21)) with the fourth co-energy variable (equation(28)). Equation (23) gives the total kinetic energy of the system which includes the internal translational and rotational momentum of the rod.

$$\begin{aligned}\mathcal{T} &= \frac{1}{2} \int_0^L \left[ \frac{1}{\rho A} \mathbf{x}_2^2 + (\rho \mathbf{J})^{-1} \mathbf{x}_4^2 \right] ds \\ &= \frac{1}{2} \int_0^L [\rho A \mathbf{q}^2 + \rho \mathbf{J} \boldsymbol{\omega}^2] ds\end{aligned}\tag{23}$$

As mentioned before the resulting total energy is the sum of equation (22) and equation (23) for obtaining equation (24).

$$\begin{aligned}\mathcal{H} &= \frac{1}{2} \int_0^L [\mathbf{K}_{se} \mathbf{x}_1^2 + \mathbf{K}_{bt} \mathbf{x}_3^2 + \frac{1}{\rho A} \mathbf{x}_2^2 + (\rho \mathbf{J})^{-1} \mathbf{x}_4^2] ds \\ &= \frac{1}{2} \int_0^L [(\mathbf{K}_{se}(\mathbf{v} - \mathbf{v}^*))^2 + \mathbf{K}_{bt}(\mathbf{u} - \mathbf{u}^*)^2 + \rho A \mathbf{q}^2 + \rho \mathbf{J} \boldsymbol{\omega}^2] ds\end{aligned}\tag{24}$$

For each energy variable there is an associated co-energy variable chosen from the Hamiltonian. The first one, presented in equation (25) is also related with the shear and elongation of the rod. The second one, related with the internal translational momentum is shown in equation (26).

$$\mathbf{e}_1 = \mathbf{K}_{se} \mathbf{x}_1 = \mathbf{K}_{se}(\mathbf{v} - \mathbf{v}^*)\tag{25}$$

$$\mathbf{e}_2 = \frac{1}{\rho A} \mathbf{x}_2 = \frac{1}{\rho A} \rho A \mathbf{q} = \mathbf{q}\tag{26}$$

The third one, related with the bending and torsion is shown in equation (27). In the same way, the fourth co-energy variable presented in equation (28) is related to the internal internal rotational momentum giving as result  $\boldsymbol{\omega}$ .

$$\mathbf{e}_3 = \mathbf{K}_{bt} \mathbf{x}_3 = \mathbf{K}_{bt}(\mathbf{u} - \mathbf{u}^*)\tag{27}$$

$$\mathbf{e}_4 = (\rho \mathbf{J})^{-1} \mathbf{x}_4 = (\rho \mathbf{J})^{-1} \rho \mathbf{J} \boldsymbol{\omega} = \boldsymbol{\omega}\tag{28}$$

### 3.1.1 Port Hamiltonian model

In this section the  $(\dot{\cdot})$  symbol above the  $x$  is introduced to present the derivative with respect to  $t$  of each state variable. These derivatives relate the co-energy variables and the energy variables one to each other. Equation (29) gives the time derivative of  $\mathbf{x}_1$  by solving equation (15) for  $\mathbf{v}_t$ . The time derivative of  $\mathbf{x}_2$  is shown in equation (30) by solving the balance equation (9) for  $\rho A \mathbf{q}_t$ .

$$\begin{aligned}\dot{\mathbf{x}}_1 &= \mathbf{v}_t = \mathbf{q}_s + \hat{\mathbf{u}}\mathbf{q} - \hat{\mathbf{v}}\boldsymbol{\omega} = \left(\frac{\partial}{\partial s} + \hat{\mathbf{u}}\right)\mathbf{q} + \hat{\mathbf{v}}\boldsymbol{\omega} \\ \dot{\mathbf{x}}_1 &= \left(\frac{\partial}{\partial s} + \hat{\mathbf{u}}\right)\mathbf{e}_2 + \hat{\mathbf{v}}\mathbf{e}_4\end{aligned}\quad (29)$$

$$\begin{aligned}\dot{\mathbf{x}}_2 &= \rho A \mathbf{q}_t = \mathbf{R}^T \mathbf{n}_s - \rho A \hat{\boldsymbol{\omega}} \mathbf{q} + \mathbf{R}^T \mathbf{f} \\ \dot{\mathbf{x}}_2 &= \mathbf{R}^T \mathbf{R}_s \mathbf{K}_{se}(\mathbf{v} - \mathbf{v}^*) + \mathbf{R}^T \mathbf{R} \frac{\partial}{\partial s} \mathbf{K}_{se}(\mathbf{v} - \mathbf{v}^*) - \rho A \hat{\boldsymbol{\omega}} \mathbf{q} + \mathbf{R}^T \mathbf{f} \\ \dot{\mathbf{x}}_2 &= \mathbf{R}^T \mathbf{R} \hat{\mathbf{u}} \mathbf{K}_{se}(\mathbf{v} - \mathbf{v}^*) + \mathbf{R}^T \mathbf{R} \frac{\partial}{\partial s} \mathbf{K}_{se}(\mathbf{v} - \mathbf{v}^*) - \rho A \hat{\boldsymbol{\omega}} \mathbf{q} + \mathbf{R}^T \mathbf{f} \\ \dot{\mathbf{x}}_2 &= \left(\frac{\partial}{\partial s} + \hat{\mathbf{u}}\right)\mathbf{e}_1 - \rho A \hat{\boldsymbol{\omega}} \mathbf{e}_2 + \mathbf{R}^T \mathbf{f}\end{aligned}\quad (30)$$

Equation (31) gives the time derivative of  $\mathbf{x}_3$  by solving equation (16) for  $\mathbf{u}_t$ . The time derivative of  $\mathbf{x}_4$  is shown in equation (32) by solving the balance equation (10) for  $\rho \mathbf{J} \boldsymbol{\omega}_t$ .

$$\begin{aligned}\dot{\mathbf{x}}_3 &= \mathbf{u}_t = \boldsymbol{\omega}_s + \hat{\mathbf{u}}\boldsymbol{\omega} = \left(\frac{\partial}{\partial s} + \hat{\mathbf{u}}\right)\boldsymbol{\omega} \\ \dot{\mathbf{x}}_3 &= \left(\frac{\partial}{\partial s} + \hat{\mathbf{u}}\right)\mathbf{e}_4\end{aligned}\quad (31)$$

$$\begin{aligned}\dot{\mathbf{x}}_4 &= \rho \mathbf{J} \boldsymbol{\omega}_t = \mathbf{R}^T \mathbf{m}_s - \rho \hat{\boldsymbol{\omega}} \mathbf{J} \boldsymbol{\omega} + \mathbf{R}^T \hat{\boldsymbol{\rho}}_s \mathbf{n} + \mathbf{R}^T \mathbf{l} \\ \dot{\mathbf{x}}_4 &= \mathbf{R}^T \mathbf{R}_s \mathbf{K}_{bt}(\mathbf{u} - \mathbf{u}^*) + \mathbf{R}^T \mathbf{R} \frac{\partial}{\partial s} \mathbf{K}_{bt}(\mathbf{u} - \mathbf{u}^*) - \rho \hat{\boldsymbol{\omega}} \mathbf{J} \boldsymbol{\omega} + \mathbf{R}^T \hat{\boldsymbol{\rho}}_s \mathbf{R} \mathbf{K}_{se}(\mathbf{v} - \mathbf{v}^*) + \mathbf{R}^T \mathbf{l} \\ \dot{\mathbf{x}}_4 &= \mathbf{R}^T \mathbf{R} \hat{\mathbf{u}} \mathbf{K}_{bt}(\mathbf{u} - \mathbf{u}^*) + \mathbf{R}^T \mathbf{R} \frac{\partial}{\partial s} \mathbf{K}_{bt}(\mathbf{u} - \mathbf{u}^*) - \rho \hat{\boldsymbol{\omega}} \mathbf{J} \boldsymbol{\omega} + \hat{\mathbf{v}} \mathbf{K}_{se}(\mathbf{v} - \mathbf{v}^*) + \mathbf{R}^T \mathbf{l} \\ \dot{\mathbf{x}}_4 &= \left(\frac{\partial}{\partial s} + \hat{\mathbf{u}}\right)\mathbf{e}_3 - \rho \hat{\boldsymbol{\omega}} \mathbf{J} \mathbf{e}_4 + \hat{\mathbf{v}} \mathbf{e}_1 + \mathbf{R}^T \mathbf{l}\end{aligned}\quad (32)$$

Remembering that a port Hamiltonian system could be expressed as in equation (1), the current model can be expressed in the Hamiltonian form as in equation (33). Where  $R$ , in this case are the damping or dissipation matrices.

$$\underbrace{\begin{bmatrix} \dot{x}_1 \\ \dot{x}_2 \\ \dot{x}_3 \\ \dot{x}_4 \end{bmatrix}}_{\dot{\mathbf{x}}_{rod}} = \underbrace{\begin{bmatrix} 0 & \frac{\partial}{\partial s} & 0 & 0 \\ \frac{\partial}{\partial s} & 0 & 0 & 0 \\ 0 & 0 & 0 & \frac{\partial}{\partial s} \\ 0 & 0 & \frac{\partial}{\partial s} & 0 \end{bmatrix}}_{J_{rod}} + \underbrace{\begin{bmatrix} 0 & \hat{\mathbf{u}} & 0 & \hat{\mathbf{v}} \\ \hat{\mathbf{u}} & -\rho A \hat{\boldsymbol{\omega}} & 0 & 0 \\ 0 & 0 & 0 & \hat{\mathbf{u}} \\ \hat{\mathbf{v}} & 0 & \hat{\mathbf{u}} & -\rho \mathbf{J} \hat{\boldsymbol{\omega}} \end{bmatrix}}_{R_{rod}} - \underbrace{\begin{bmatrix} 0 & 0 & 0 & 0 \\ 0 & \mathbf{B}_{se} & 0 & 0 \\ 0 & 0 & 0 & 0 \\ 0 & 0 & 0 & \mathbf{B}_{bt} \end{bmatrix}}_{R_{rod}} \underbrace{\begin{bmatrix} \mathbf{e}_1 \\ \mathbf{e}_2 \\ \mathbf{e}_3 \\ \mathbf{e}_4 \end{bmatrix}}_{\mathbf{e}_{rod}} + \underbrace{\begin{bmatrix} 0 & 0 \\ \mathbf{R}^T & 0 \\ 0 & 0 \\ 0 & \mathbf{R}^T \end{bmatrix}}_{g_{rod}} \underbrace{\begin{bmatrix} \mathbf{f} \\ \mathbf{l} \end{bmatrix}}_{\mathbf{u}_{rod}} \quad (33)$$

With:

$$\begin{bmatrix} \mathbf{e}_1 \\ \mathbf{e}_2 \\ \mathbf{e}_3 \\ \mathbf{e}_4 \end{bmatrix} = \mathcal{L}\mathbf{x} = \begin{bmatrix} \mathbf{K}_{se} & 0 & 0 & 0 \\ 0 & \frac{1}{\rho A} & 0 & 0 \\ 0 & 0 & \mathbf{K}_{bt} & 0 \\ 0 & 0 & 0 & (\rho \mathbf{J})^{-1} \end{bmatrix} \begin{bmatrix} \mathbf{x}_1 \\ \mathbf{x}_2 \\ \mathbf{x}_3 \\ \mathbf{x}_4 \end{bmatrix}$$

For this project, a boundary controller should be designed, this means that the matrices  $g$  and  $u$  should be changed to have a set of boundary port variables instead of distributed parameters. To do this, the distributed forces and momentums are neglected. The vector of boundary flows and efforts is shown in equation (34) [9]. The input boundary conditions were all set to 0 except for  $\mathbf{e}_0^2$  which is the velocity at the rod's base. These variables will be explained with detail in section 4. With the changes made, the complete model is presented in equation (35).

$$\begin{bmatrix} \mathbf{f}_\partial \\ \mathbf{e}_\partial \end{bmatrix} = \begin{bmatrix} \mathbf{e}_0^2 \\ \mathbf{e}_L^1 \\ \mathbf{e}_0^4 \\ \mathbf{e}_L^3 \\ \mathbf{e}_L^2 \\ \mathbf{e}_0^1 \\ \mathbf{e}_L^4 \\ \mathbf{e}_0^3 \end{bmatrix} \quad (34)$$

$$\underbrace{\begin{bmatrix} \dot{x}_1 \\ \dot{x}_2 \\ \dot{x}_3 \\ \dot{x}_4 \end{bmatrix}}_{\dot{x}_{rod}} = \left[ \underbrace{\begin{bmatrix} 0 & \frac{\partial}{\partial s} & 0 & 0 \\ \frac{\partial}{\partial s} & 0 & 0 & 0 \\ 0 & 0 & 0 & \frac{\partial}{\partial s} \\ 0 & 0 & \frac{\partial}{\partial s} & 0 \end{bmatrix}}_{J_{rod}} + \underbrace{\begin{bmatrix} 0 & \hat{u} & 0 & \hat{v} \\ \hat{u} & -\rho A \hat{\omega} & 0 & 0 \\ 0 & 0 & 0 & \hat{u} \\ \hat{v} & 0 & \hat{u} & -\rho \mathbf{J} \hat{\omega} \end{bmatrix}}_{J_{rod}} - \underbrace{\begin{bmatrix} 0 & 0 & 0 & 0 \\ 0 & \mathbf{B}_{se} & 0 & 0 \\ 0 & 0 & 0 & 0 \\ 0 & 0 & 0 & \mathbf{B}_{bt} \end{bmatrix}}_{R_{rod}} \right] \begin{bmatrix} \mathbf{e}_1 \\ \mathbf{e}_2 \\ \mathbf{e}_3 \\ \mathbf{e}_4 \end{bmatrix} + \underbrace{\begin{bmatrix} g1 \\ g2 \\ g3 \\ g4 \end{bmatrix}}_{g_{rod}} \underbrace{\begin{bmatrix} \mathbf{e}_0^2 \\ \mathbf{e}_L^1 \\ \mathbf{e}_0^4 \\ \mathbf{e}_L^3 \end{bmatrix}}_{u_{rod}} \quad (35)$$

$$\underbrace{\begin{bmatrix} y_1 \\ y_2 \\ y_3 \\ y_4 \end{bmatrix}}_{y_{rod}} = g^T \frac{\delta \mathcal{H}}{\delta x} = [g_1 \ g_2 \ g_3 \ g_4] \begin{bmatrix} \mathbf{e}_1 \\ \mathbf{e}_2 \\ \mathbf{e}_3 \\ \mathbf{e}_4 \end{bmatrix}$$

### 3.2 Port Hamiltonian system of the piezoelectric tube actuator

The actuator for the continuum robot is a 2 pair of electrodes piezoelectric tube. In order to compute the boundary controller, the piezoelectric tube actuator was also modeled in a PHS approach as a simple mechanical spring-mass-damper system as shown in Figure 9. a voltage dependant force  $\mathbf{F}_{PZT}$  is applied to generate a displacement and an opposite force from the rod  $\mathbf{F}_{rod} = e_0^1$  is present. Also a stiffness coefficient  $\mathbf{K}$  and a damping coefficient  $\mathbf{b}$  were taken into account.

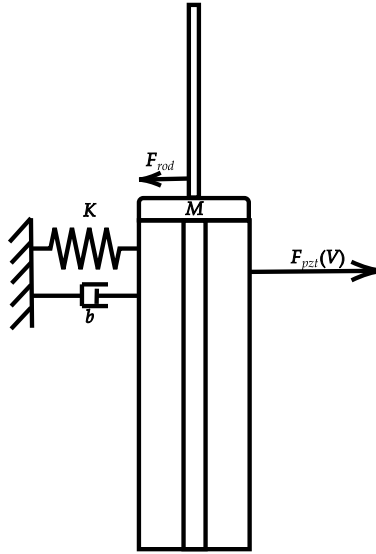


**Figure 9:** Piezoelectric tube as a Spring-Mass-Damper system

As in the rod's PHS model, the energy variables are chosen. For the piezoelectric tube case, the first energy variable is chosen as the position  $\mathbf{p}_{PZT}$  as in equation (36) and the second as the momentum  $\mathbf{m}_{PZT}$  as in equation (37).

$$\mathbf{x}_{p1} = \mathbf{p}_{PZT} \quad (36)$$

$$\mathbf{x}_{p2} = \mathbf{m}_{PZT} \quad (37)$$

Then the Hamiltonian of the system could be expressed as in equation (38) from which the co-energy variables could be extracted. These co-energy variables,  $\mathbf{K}(\mathbf{p}_{PZT})$  and  $\frac{1}{M}(\mathbf{m}_{PZT})$ , are expressed in equations (39) and (40) respectively.

$$\begin{aligned} \mathcal{H} &= \frac{1}{2}[\mathbf{K}\mathbf{x}_1^2 + \frac{1}{M}\mathbf{x}_2^2] \\ &= \frac{1}{2}[\mathbf{K}\mathbf{p}_{PZT}^2 + \frac{1}{M}\mathbf{m}_{PZT}^2] \end{aligned} \quad (38)$$



$$\mathbf{e}_{p1} = \mathbf{K} \mathbf{x}_1 = \mathbf{K}(\mathbf{p}_{pzt}) \quad (39)$$

$$\mathbf{e}_{p2} = \frac{1}{M} \mathbf{x}_2 = \frac{1}{M}(\mathbf{m}_{pzt}) = \mathbf{q}_{pzt} \quad (40)$$

### 3.2.1 Port Hamiltonian model

Hence, the piezoelectric tube actuator PHS model could be expressed as in equation (41). Where the output of the system is the actual boundary velocity,  $\mathbf{e}_0^2$  at the optical fiber's base that is needed to move the rod.

$$\underbrace{\begin{bmatrix} \dot{x}_{p1} \\ \dot{x}_{p2} \end{bmatrix}}_{\dot{\mathbf{x}}_{pzt}} = \left[ \underbrace{\begin{bmatrix} 0 & 1 \\ -1 & 0 \end{bmatrix}}_{J_{pzt}} - \underbrace{\begin{bmatrix} 0 & 0 \\ 0 & -b \end{bmatrix}}_{R_{pzt}} \right] \underbrace{\begin{bmatrix} \mathbf{e}_{p1} \\ \mathbf{e}_{p2} \end{bmatrix}}_{\mathbf{e}_{pzt}} + \underbrace{\begin{bmatrix} 0 \\ 1 \end{bmatrix}}_{g_{pzt}} \underbrace{\begin{bmatrix} \mathbf{F}(v) \end{bmatrix}}_{u_{pzt}} - \underbrace{\begin{bmatrix} 0 \\ 1 \end{bmatrix}}_{\mathbf{1}} \underbrace{\begin{bmatrix} \mathbf{F}_{rod} \end{bmatrix}}_{u_{pzt-rod}} \quad (41)$$

$$\underbrace{y}_{y_{pzt}} = g^T \frac{\delta \mathcal{H}}{\delta x} = [0 \quad 1] \begin{bmatrix} \mathbf{e}_{p1} \\ \mathbf{e}_{p2} \end{bmatrix} = \mathbf{q}_{pzt}$$

### 3.3 Interconnected model

To have a complete interconnected system the input variables and the output variables were defined [9]. Equation (42) corresponds to the input variable which includes the boundary conditions for  $\mathbf{e}_L^1$ ,  $\mathbf{e}_0^4$  and  $\mathbf{e}_L^3$ . Then, in equation (43), corresponds to the input variable of the velocity  $\mathbf{e}_0^2$  that the actuator exerts at the base of the rod.

$$\mathcal{U}_1 = \mathcal{W}_{B1} \begin{bmatrix} \mathbf{f}_\partial \\ \mathbf{e}_\partial \end{bmatrix} = 0 \quad (42)$$

$$\mathcal{W}_{B1} = \begin{bmatrix} 0 & 1 & 0 & 0 & 0 & 0 & 0 & 0 \\ 0 & 0 & 1 & 0 & 0 & 0 & 0 & 0 \\ 0 & 0 & 0 & 1 & 0 & 0 & 0 & 0 \end{bmatrix}$$

$$\mathcal{U}_2 = \mathcal{W}_{B2} \begin{bmatrix} \mathbf{f}_\partial \\ \mathbf{e}_\partial \end{bmatrix} = \mathbf{e}_0^2 \quad (43)$$

$$\mathcal{W}_{B1} = [1 \quad 0 \quad 0 \quad 0 \quad 0 \quad 0 \quad 0 \quad 0]$$

The first output variable could be expressed as in equation (44) which corresponds to  $e_L^2$ ,  $e_L^4$  and  $e_0^3$ . Finally, equation (45) corresponds to the output  $e_0^1$  which is the force that the rod exerts in the actuator.

$$\mathcal{Y}_1 = \mathcal{W}_{C1} \begin{bmatrix} \mathbf{f}_\partial \\ \mathbf{e}_\partial \end{bmatrix} \quad (44)$$

$$\mathcal{W}_{C1} = \begin{bmatrix} 0 & 0 & 0 & 0 & 1 & 0 & 0 & 0 \\ 0 & 0 & 1 & 0 & 0 & 0 & 1 & 0 \\ 0 & 0 & 0 & 1 & 0 & 0 & 0 & 1 \end{bmatrix}$$

$$\mathcal{Y}_2 = \mathcal{W}_{C2} \begin{bmatrix} \mathbf{f}_\partial \\ \mathbf{e}_\partial \end{bmatrix} = \mathcal{C} \mathbf{e}_0^1 \quad (45)$$

$$\mathcal{W}_{C1} = [0 \ 0 \ 0 \ 0 \ 0 \ 1 \ 0 \ 0]$$

The infinite dimensional interconnected PHS model could be expressed in equation (46) with  $g_i = [0 \ 0 \ 0 \ 0 \ 0 \ 1]^T$ .

$$\begin{bmatrix} \dot{\mathbf{x}}_{rod} \\ \dot{\mathbf{x}}_{pzt} \end{bmatrix} = \begin{bmatrix} (J_{rod} - R_{rod}) & | & 0 \\ \mathcal{C} & | & (J_{pzt} - R_{pzt}) \end{bmatrix} \begin{bmatrix} \mathbf{e}_{rod} \\ \mathbf{e}_{pzt} \end{bmatrix} + g_i [\mathbf{F}(V)] \quad (46)$$

## 4 Rod's numerical resolution and validation

### 4.1 Spatial discretization

For the next section an spatial discretization for the first part of the model presented in equation (47) is made as in [10] and [11] where the concept of staggered grids is introduced as the notation used.

$$\begin{bmatrix} \mathbf{f}_1 \\ \mathbf{f}_2 \\ \mathbf{f}_3 \\ \mathbf{f}_4 \end{bmatrix} = \begin{bmatrix} 0 & \frac{\partial}{\partial s} & 0 & 0 \\ \frac{\partial}{\partial s} & 0 & 0 & 0 \\ 0 & 0 & 0 & \frac{\partial}{\partial s} \\ 0 & 0 & \frac{\partial}{\partial s} & 0 \end{bmatrix} \begin{bmatrix} \mathbf{e}_1 \\ \mathbf{e}_2 \\ \mathbf{e}_3 \\ \mathbf{e}_4 \end{bmatrix} \quad (47)$$

First a spatial resolution  $h$  is introduced where an  $n$  number of elements can be found such that  $(n + \frac{1}{2})h = L$ . The first part of the system is discretized over the grid presented in Figure 10 for  $\mathbf{x}_1$  and  $\mathbf{x}_2$  and the grid presented in in Figure 11 for  $\mathbf{x}_1$  and  $\mathbf{x}_4$ . The spatial discretization is made for a clamped-free rod.

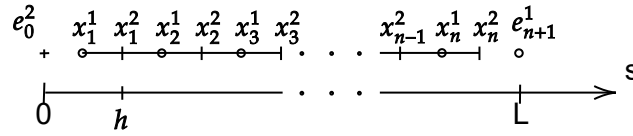


Figure 10: 1D Staggered Grid for  $\mathbf{x}_{dis}^1$  and  $\mathbf{x}_{dis}^2$

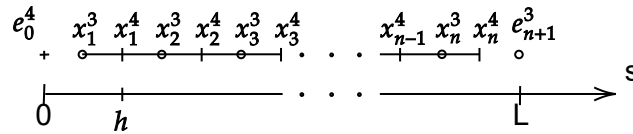


Figure 11: 1D Staggered Grid for  $\mathbf{x}_{dis}^3$  and  $\mathbf{x}_{dis}^4$

In this discretized model, the state variables are changed by a finite-dimensional vector  $\mathbf{x}_{dis} = [x_{dis}^1 \ x_{dis}^2 \ x_{dis}^3 \ x_{dis}^4]^T \in \mathbb{R}^{2n}$  with  $\mathbf{x}_{dis}^1 = [x_1^1 \dots x_n^1]^T$ ,  $\mathbf{x}_{dis}^2 = [x_1^2 \dots x_n^2]^T$ ,  $\mathbf{x}_{dis}^3 = [x_1^3 \dots x_n^3]^T$  and  $\mathbf{x}_{dis}^4 = [x_1^4 \dots x_n^4]^T$ , where the  $\mathbf{x}_k^{\{1,2,3,4\}}$  ( $k \in \{1 \dots n\}$ ) are the approximations of the state variables respectively evaluated at  $s = \{(k-1)h, (k-0.5)h\}$  with  $n$  as the internal grid points. Then,  $e_0^2$ ,  $e_0^4$ ,  $e_{n+1}^1$  and  $e_{n+1}^3$  denote the boundary conditions at the base and at the tip of the rod.

The vector of discrete co-energy variables could be defined as in equation (48),

$$\mathbf{e}_{dis} = \mathcal{L}_{dis} \mathbf{x}_{dis} \quad (48)$$

and from this, equation (49) could be obtained.

$$\begin{bmatrix} e_k^1 \\ e_k^2 \\ e_k^3 \\ e_k^4 \end{bmatrix} = \mathcal{L}_k \begin{bmatrix} x_k^1 \\ x_k^2 \\ x_k^3 \\ x_k^4 \end{bmatrix} \quad (49)$$

Thus, by central approximation of the spatial derivative equation (50) appears.

$$\begin{bmatrix} f_k^1 \\ f_k^2 \\ f_k^3 \\ f_k^4 \end{bmatrix} = \frac{1}{h} \begin{bmatrix} e_{k+1}^2 - e_k^2 \\ e_k^1 - e_{k-1}^1 \\ e_{k+1}^3 - e_k^3 \\ e_k^4 - e_{k-1}^4 \end{bmatrix} \quad (50)$$

where  $\mathbf{f}_{dis} = [f_{dis}^1 \ f_{dis}^2 \ f_{dis}^3 \ f_{dis}^4]^T = [f_1^1 \dots f_n^1 \ f_1^2 \dots f_n^2 \ f_1^3 \dots f_n^3 \ f_1^4 \dots f_n^4]^T$  is the approximation of equation 47.

In this way the matrices shown in equations (51) and (52) could be found for a clamped-free rod as in [12].

$$\mathbf{f}_{dis}^1 = \frac{1}{h} \underbrace{\begin{bmatrix} 1 & & & & \\ -1 & 1 & & & \\ & \ddots & \ddots & & \\ & & & -1 & 1 \end{bmatrix}}_D \mathbf{e}_{dis}^2 + \frac{1}{h} \begin{bmatrix} -1 \\ 0 \\ \vdots \\ 0 \end{bmatrix} \mathbf{e}_0^2 \quad (51)$$

$$\mathbf{f}_{dis}^2 = \frac{1}{h} \underbrace{\begin{bmatrix} -1 & 1 & & & \\ & \ddots & \ddots & & \\ & & & -1 & 1 \\ & & & & -1 \end{bmatrix}}_{-D^T} \mathbf{e}_{dis}^1 + \frac{1}{h} \begin{bmatrix} 0 \\ \vdots \\ 0 \\ 1 \end{bmatrix} \mathbf{e}_{n+1}^1 \quad (52)$$

Analogous, these matrices could be found for  $\mathbf{f}_{dis}^3$  and  $\mathbf{f}_{dis}^4$ . So the system in equation (47) could be expressed in a discretized form as in the equation (53).

$$\mathbf{f}_{dis} = \underbrace{\begin{bmatrix} 0 & D & 0 & 0 \\ -D^T & 0 & 0 & 0 \\ 0 & 0 & 0 & D \\ 0 & 0 & -D^T & 0 \end{bmatrix}}_{J_{dis}} \mathbf{e}_{dis} + \underbrace{\begin{bmatrix} g_1 \\ g_2 \\ g_3 \\ g_4 \end{bmatrix}}_{g_{dis}} \begin{bmatrix} e_0^2 \\ e_{n+1}^1 \\ e_0^4 \\ e_{n+1}^3 \end{bmatrix} \quad (53)$$

With:

$$g_1 = \frac{1}{h} \begin{bmatrix} -1 \\ 0 \\ \vdots \\ 0 \end{bmatrix} \quad g_2 = \frac{1}{h} \begin{bmatrix} 0 \\ 0 \\ \vdots \\ 1 \end{bmatrix}$$

$$g_3 = \frac{1}{h} \begin{bmatrix} -1 \\ 0 \\ \vdots \\ 0 \end{bmatrix} \quad g_4 = \frac{1}{h} \begin{bmatrix} 0 \\ 0 \\ \vdots \\ 1 \end{bmatrix}$$

This leads to the final port Hamiltonian system shown in equation (54), in which the distributed forces and momentum are neglected for controlling purposes.

$$\begin{bmatrix} \dot{x}_1 \\ \dot{x}_2 \\ \dot{x}_3 \\ \dot{x}_4 \end{bmatrix} = \underbrace{\begin{bmatrix} 0 & D & 0 & 0 \\ -D^T & 0 & 0 & 0 \\ 0 & 0 & 0 & D \\ 0 & 0 & -D^T & 0 \end{bmatrix}}_{J_{dis}} + \underbrace{\begin{bmatrix} 0 & \hat{u} & 0 & \hat{v} \\ \hat{u} & -\rho A \hat{\omega} & 0 & 0 \\ 0 & 0 & 0 & \hat{u} \\ \hat{v} & 0 & \hat{u} & -\rho J \hat{\omega} \end{bmatrix}}_{R} - \underbrace{\begin{bmatrix} 0 & 0 & 0 & 0 \\ 0 & \mathbf{B}_{se} & 0 & 0 \\ 0 & 0 & 0 & 0 \\ 0 & 0 & 0 & \mathbf{B}_{bt} \end{bmatrix}}_{R} \underbrace{\begin{bmatrix} e_1 \\ e_2 \\ e_3 \\ e_4 \end{bmatrix}}_{e_{dis}} + \underbrace{\begin{bmatrix} g_1 \\ g_2 \\ g_3 \\ g_4 \end{bmatrix}}_{g_{dis}} \underbrace{\begin{bmatrix} e_0^2 \\ e_{n+1}^1 \\ e_0^4 \\ e_{n+1}^3 \end{bmatrix}}_u \quad (54)$$

$$\begin{bmatrix} y_1 \\ y_2 \\ y_3 \\ y_4 \end{bmatrix} = g^T \frac{\delta \mathcal{H}}{\delta x} = [g_1 \ g_2 \ g_3 \ g_4] \begin{bmatrix} e_1 \\ e_2 \\ e_3 \\ e_4 \end{bmatrix}$$

#### 4.1.1 Interconnected model

Finally the complete and discretized interconnected model between the optical fiber rod and the piezoelectric tube could be expressed as in equation (55).

$$\begin{bmatrix} \dot{x}_1 \\ \dot{x}_2 \\ \dot{x}_3 \\ \dot{x}_4 \\ \dot{x}_{p1} \\ \dot{x}_{p2} \end{bmatrix} = \left[ \begin{array}{cccc|cc} 0 & D + \hat{u} & 0 & \hat{v} & 0 & g_1 \\ -D^T + \hat{u} & -\rho A \hat{\omega} - \mathbf{B}_{se} & 0 & 0 & 0 & 0 \\ 0 & 0 & 0 & D + \hat{u} & 0 & 0 \\ \hat{v} & 0 & -D^T + \hat{u} & -\rho J \omega - \mathbf{B}_{bt} & 0 & 0 \\ \hline 0 & 0 & 0 & 0 & 0 & 1 \\ -g_1^T & 0 & 0 & 0 & -1 & -\mathbf{b} \end{array} \right] \begin{bmatrix} e_1 \\ e_2 \\ e_3 \\ e_4 \\ e_{p1} \\ e_{p2} \end{bmatrix} + \begin{bmatrix} 0 \\ 0 \\ 0 \\ 0 \\ 0 \\ 1 \end{bmatrix} [\mathbf{F}(V)] \quad (55)$$

## 4.2 Numerical validation

The purpose of this section is to validate the model in equation (54) by implementing a simulation via *Matlab/Simulink* by discretizing the rod into 20 elements. The simulation model is presented in Figure (12). The PHS rod function is where the model in equation (33) is solved. In the Pt function, equation (5) is solved for  $p_t$ . The initial conditions for the integration blocks are obtained by solving equation (17) for statics by shooting method [8].

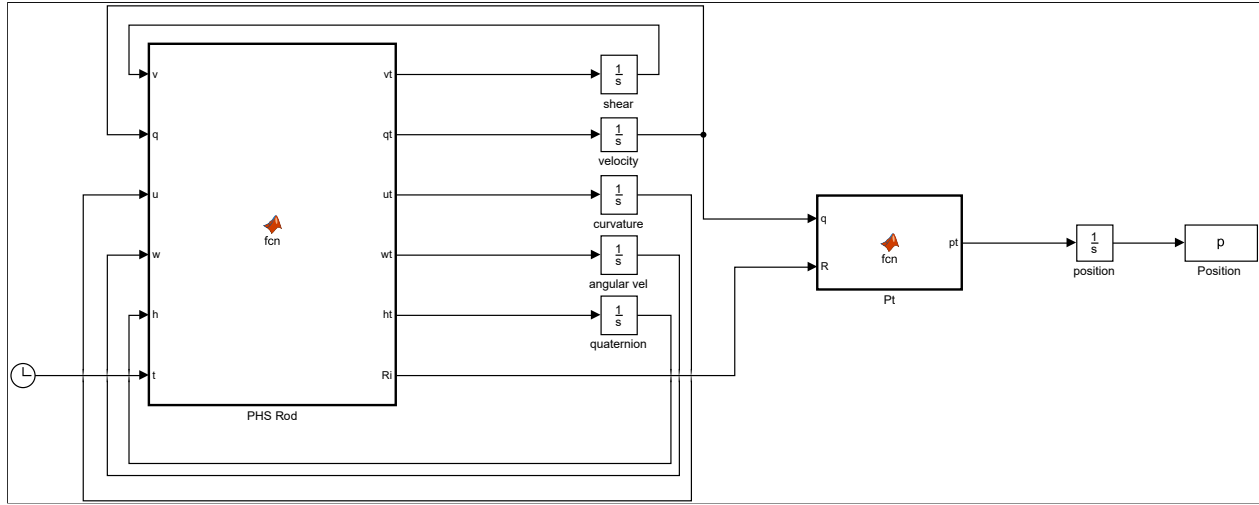
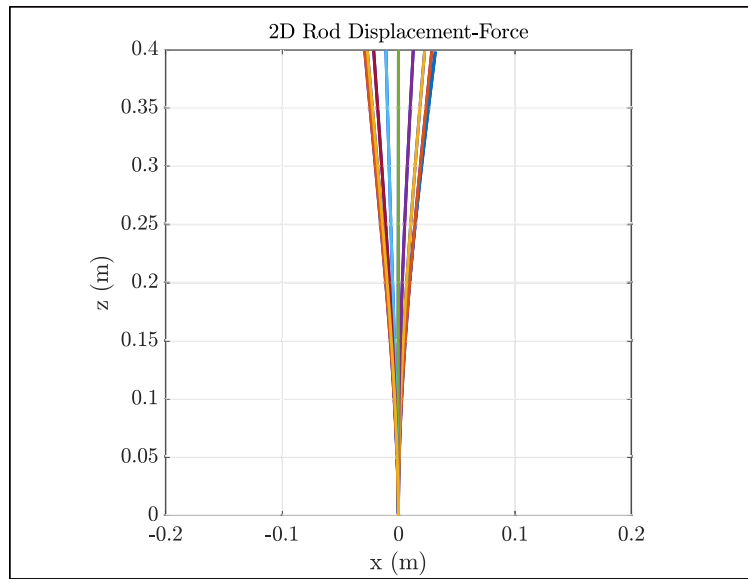


Figure 12: Simulink PHS rod's model

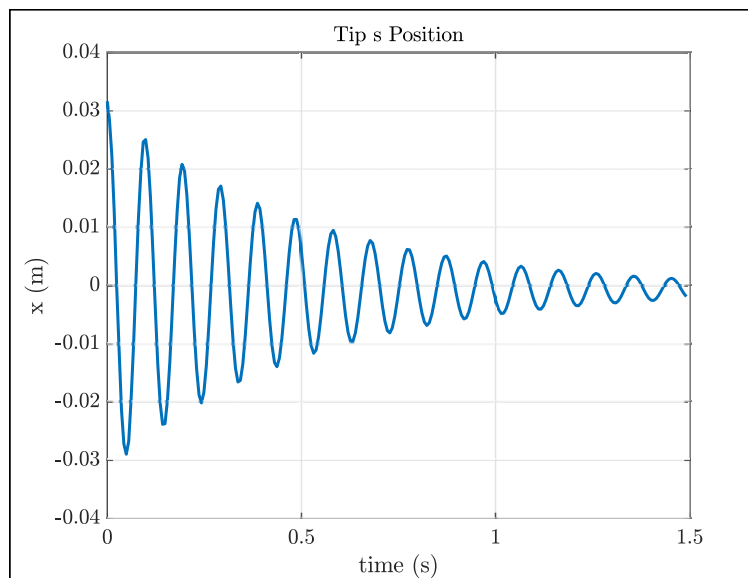
As an example, the dynamics of a cantilever rod with the parameters shown in table 4 were simulated. A force of  $[0.5 \ 0 \ 0]N$  at the tip was considered as an initial state of the rod, then, the force was released. Figure 13 shows the first few frames of the simulation. Figure 14 shows the tip's position in the 1.5s of simulation. It can be seen that the behavior is similar to the classic Cosserat rod model presented in section 2.

Table 4: Main rod's parameters

Parameter	Value	Units
Length (L)	0,4	m
Young 's modulus (E)	207	GPa
Radius (r)	0,0012	m
Density ( $\rho$ )	8000	kg/m <sup>3</sup>



**Figure 13:** A force of 0.5 N is applied to the rod's tip and then released



**Figure 14:** Tip's position with very small damping

## 5 Experimental setup and parameters identification

### 5.1 Equipment

To perform the experimental implementation the components listed below were used.

- 1 *PT230.94* PT Piezo Scanner Tube
- 1 5cm Long optical fiber piece
- 2 *LC-2420* Keyence ultra high accuracy laser displacement meter
- 1 *A400DI* Voltage amplifier
- 1 *CP1104* dSpace controller board
- 1 *Newport* Optical table

### 5.2 CAD model

The experimental part needed a base for the piezoelectric tube, and a base for the sensors. The pieces were designed in the software *Auto Desk Inventor Professional 2022*. For the actuator base, a four legged small base was designed as shown in the render of Figure 15a. For the sensors, a four degrees adjustable support was designed as shown in the render of 15b.

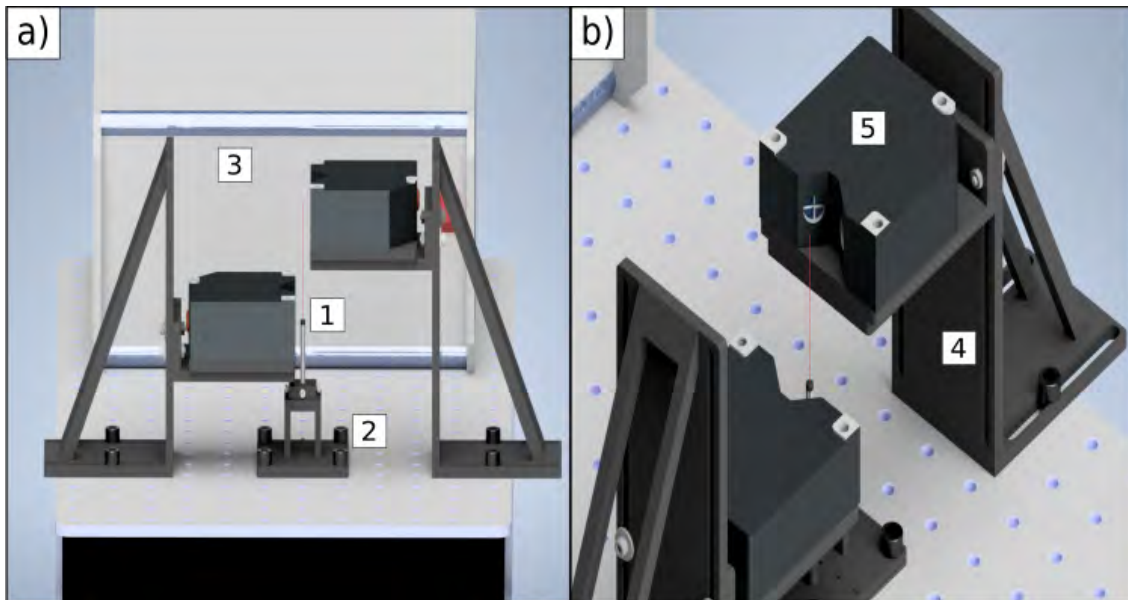


**Figure 15:** a) 1: Continuum robot; 2: four legged base; 3: A400DI voltage amplifier. b) 4: four degrees adjustable support; 5: Keyence sensor



### 5.3 Experimental setup

The piezoelectric tube base was printed in a resin material to have a better material resolution. The piezoelectric tube is a very delicate component moved through a voltage. This voltage was applied by making contact to the electrodes with screws connected to the voltage amplifier. The contact with the screws could cause some damage to the tube if a strong force is applied to them when adjusting. To reduce the risk, the base was designed with a small tube as shown in Figure 16a, the cable that passes through the middle is connected to ground. This little tube helps to reduce the force of the screws. In Figure 16b, a piezoelectric foil touching the ground cable is added to this base tube to avoid current peaks when the voltage is applied. Then in 16c the inserted piezoelectric tube can be appreciated. The screws make contact with each of the four electrodes. Finally, in 16d a small holder was designed to maintain the optic fiber centered and fixed.

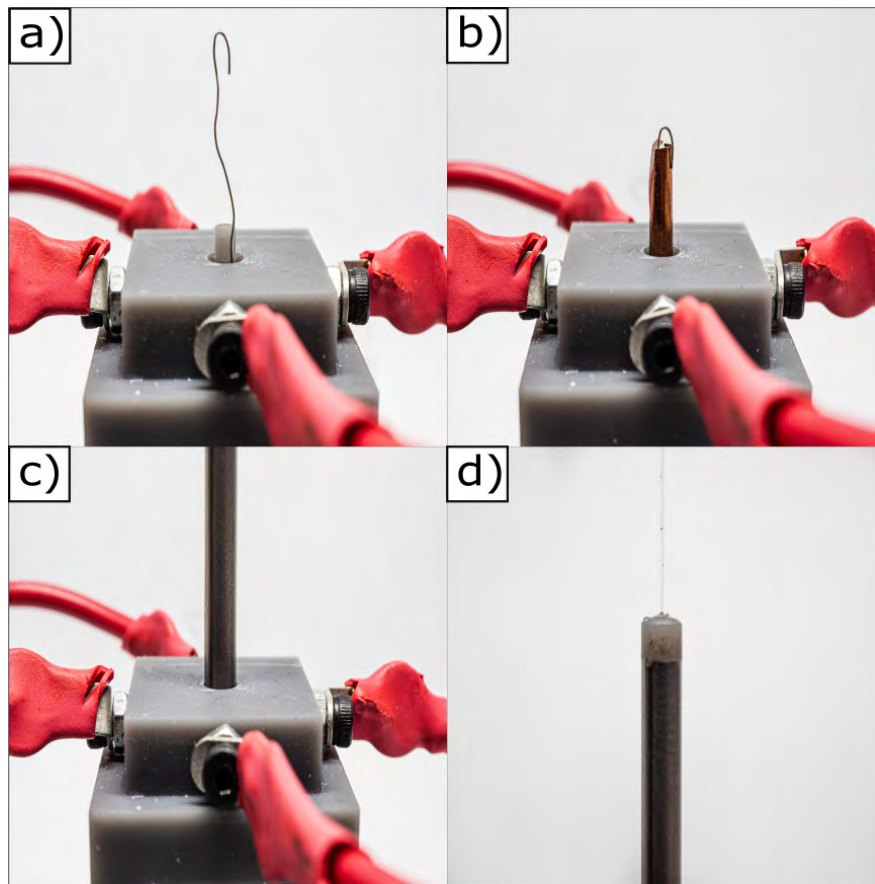


**Figure 16:** a) Inside support tube; b) Piezoelectric sheet; c) Piezoelectric tube inserted; d) Optical fiber holder

The supports for the displacement sensors were printed in PLA material for a 3D printing machine. The complete experimental setup can be appreciated in Figure 17a. For measuring the position of either the actuator and the optical fiber, the Keyence sensors send a laser

spot that bounces in the surface of the measured component as shown in Figure 17b.

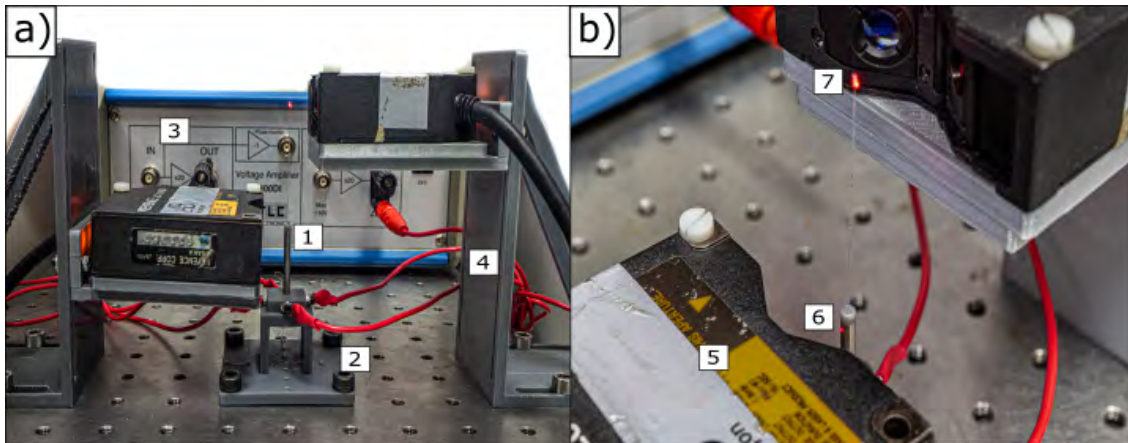


**Figure 17:** a) 1: Continuum robot; 2: four legged base; 3: A400DI voltage amplifier; 4: four degrees adjustable support. b) 5: Keyence LC-2420 sensor; 6: Actuator's displacement laser spot; 7: Optical fiber's displacement laser spot

## 5.4 Optical fiber parameters identification

In order to have an accurate model, some parameters were identified. To do this, some experimental measurements of the rod's tip displacement were performed. This measurements were performed with a MEMS Analyzer *Polytec MSA-500*. This machine measured the displacement using a laser. Figure 18 shows the setup in the MEMS table used to perform the experiments. The measurements where made using a 2X microscope objective, the 3D printed base with the piezoelectric tube and a 5cm long optic fiber.

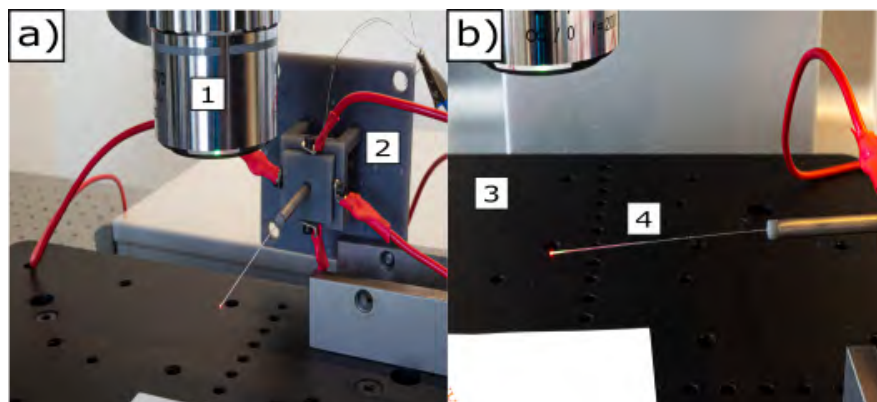


**Figure 18:** a) 1: Mitutoyo 2X Objective; 2: 3D printed base. b) 3: X and y moving table; 4: 5cm optic fiber and piezoelectric tube

To obtain accurate measurements, the scheme shown in Figure 19 was implemented. In 19a, an Arduino UNO was programmed with a simple code to send 3, 4 and 5 volts to a 20X voltage amplifier to obtain 60, 80 and 100 volts respectively to move the tube and the optical fiber to an initial position. Then in 19b, this applied voltage was turned off (0 volts), and simultaneously, a TTL signal was sent to the MEMS analyzer. This TTL signal was used as a trigger to make a measurement as shown in 19c. The 0 volts of the applied voltage, released the optic fiber as in 19d.

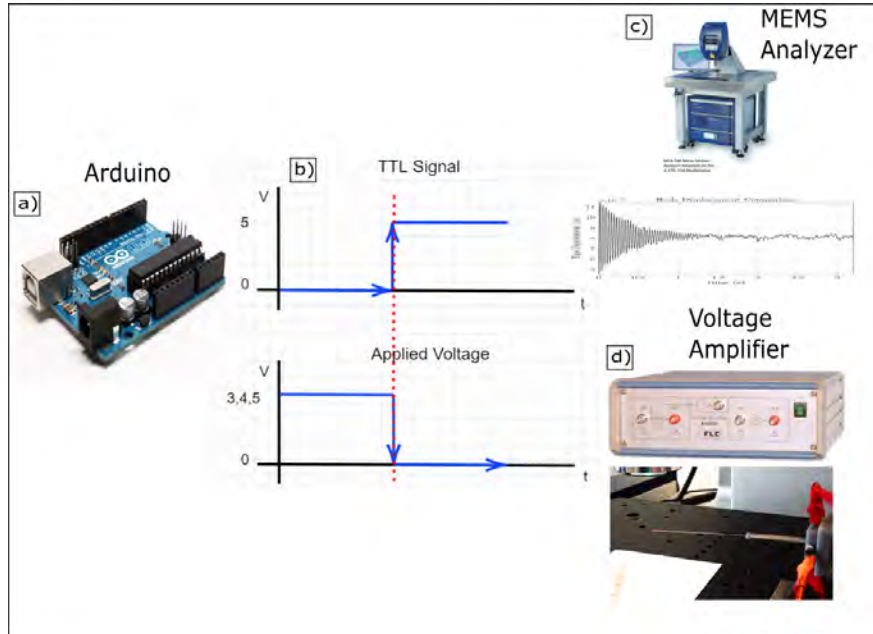


**Figure 19:** a) Arduino UNO; b) Simultaneous signals (trigger and voltage signals); c) MEMS measurement; d) Release of the initial position

Figure 20 shows the comparison of the measurements for the 3 different applied voltages. It can be appreciated that the system's response is consistent, the amplitude of the displacement grows when the voltage changes and the damping is always the same.

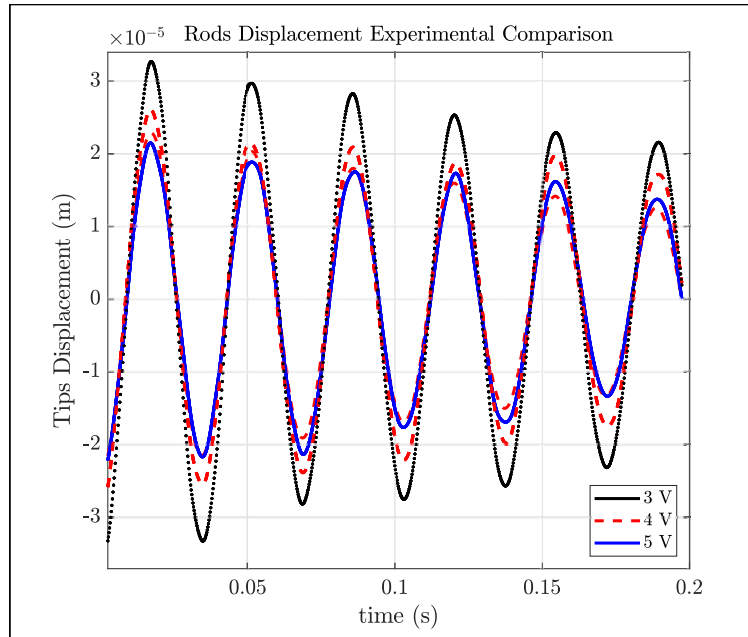


**Figure 20:** Tip's experimental displacement comparison

Then, the parameters shown in table 5 were left fixed in order to have the same frequency of the rod's tip in the experimental measurements and the *Matlab* simulation. Hence, the only parameters to be identified were the dissipation terms of the system, the damping matrices. They were identified by the use of the function *fsolve* and the *Levenberg-Marquardt* algorithm to reduce the error between measurements and the simulation.

**Table 5:** Fixed Parameters

Parameter	Value	Units
Young 's modulus (E)	9	GPa
Radius (r)	126	$\mu\text{m}$
Density ( $\rho$ )	1930	$\text{kg}/\text{m}^3$

The displacement obtained for the 5V input (Figure 21a) was used to identify the required parameters. These parameters are shown in table 7. After the identification, the measurements of 3V and 4V were used to validate these new parameters as shown in Figure 21b and 21c respectively. Finally a comparison between the three simulations was made in Figure 21d.

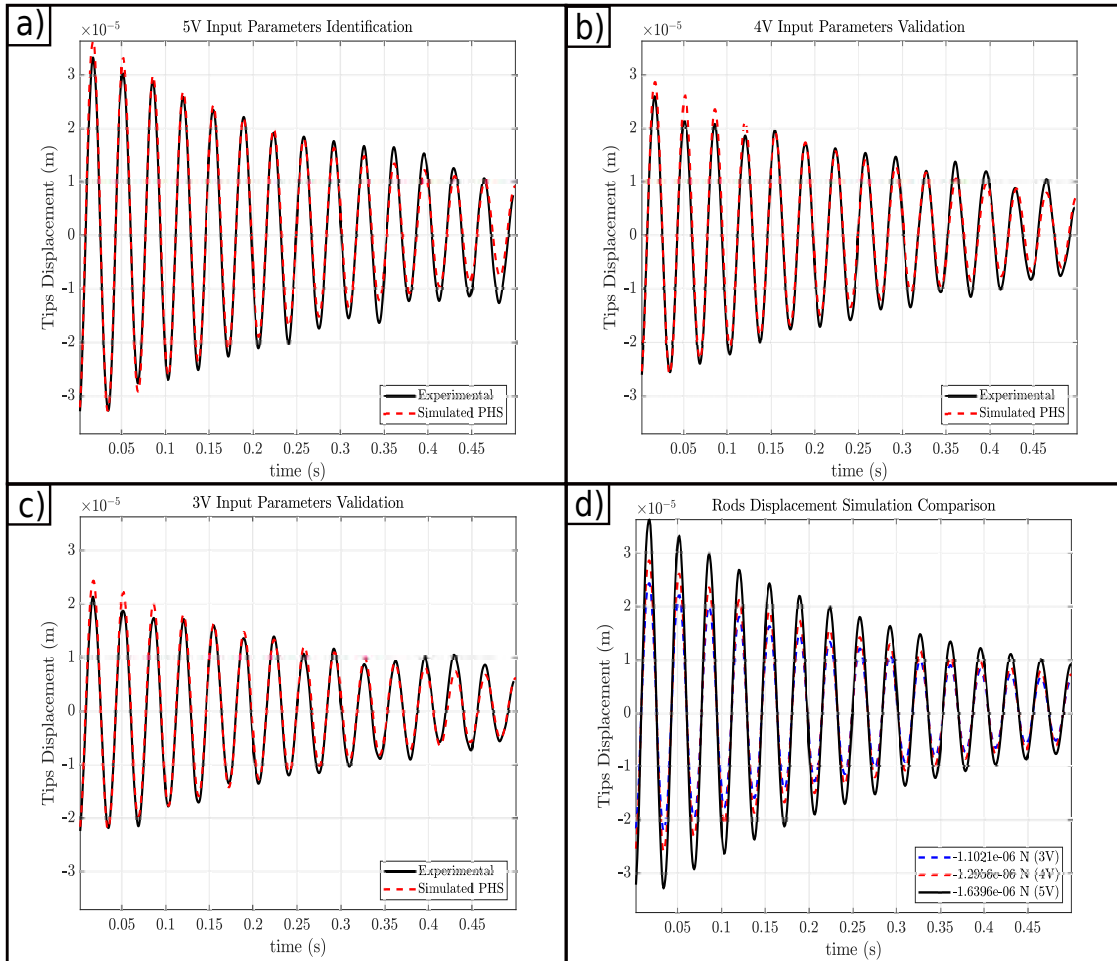


**Figure 21:** a) 5V input used for identification; b) 4V input for validation; c) 3V input for validation; d) Simulation comparison and validation

**Table 6:** Identified optical fiber's parameters

Parameter	Value
$B_{se}$	$\begin{bmatrix} 1.0883e-06 & 0 & 0 \\ 0 & 9.9051e-07 & 0 \\ 0 & 0 & 6.0282e-07 \end{bmatrix}$
$B_{bt}$	$\begin{bmatrix} 4.6677e-07 & 0 & 0 \\ 0 & 3.4323e-07 & 0 \\ 0 & 0 & 1.3407e-06 \end{bmatrix}$

Figure 22 shows the first frames of the rod's behavior when a force of  $-1.6396 \mu N$  at the tip is applied and released. Then in Figure 23, the displacement and damping of the tip is appreciated in a 1.5s simulation.

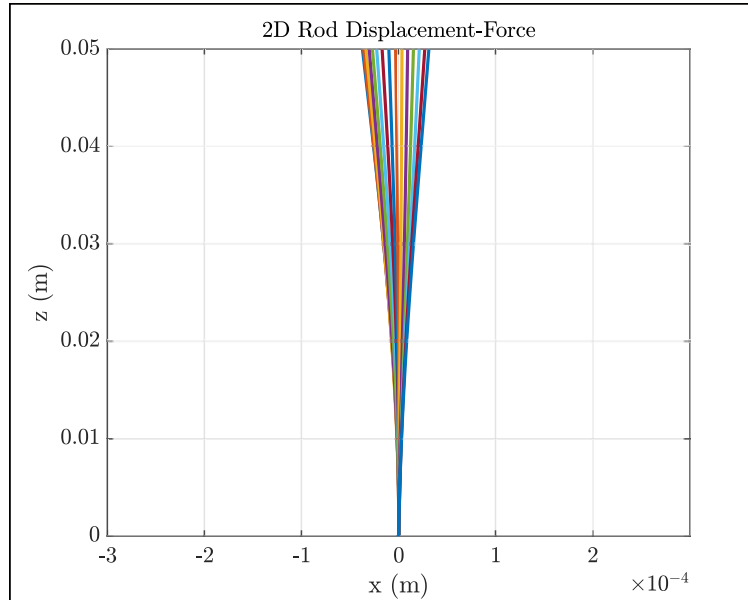


**Figure 22:** A force of  $-1.6396 \mu N$  is applied to the rod's tip and then released.

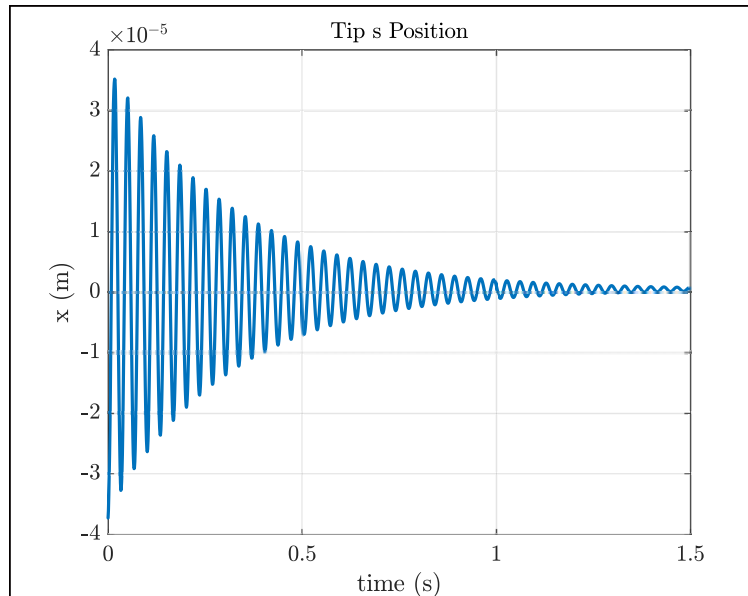


**Figure 23:** Tip's position with the identified damping

## 5.5 Piezoelectric tube parameters identification

Same as the optical fiber, some physical parameters were identified for the actuator. In this case, the mass of the piezoelectric tube with the optical fiber holder, was approximately 1g, so the parameters to be identified were the stiffness  $\mathbf{K}$ , the damping  $\mathbf{b}$  and a force coefficient that will give the necessary voltage to move the piezoelectric tube. In order to identify these parameters, an step input voltage of 200V was applied to the actuator, then with the help of the *Matlab* function *lsqcurvefit* the best fitting parameters were identified. Figure 24 shows the result of the fitting simulated response in the experimental data curve. The parameters are shown in table 7.

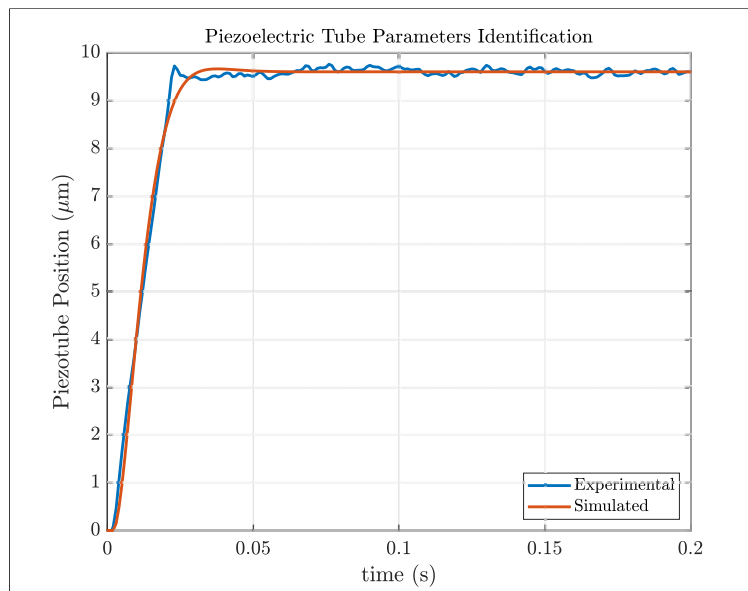


**Figure 24:** Curve fitting for piezoelectric tube parameters identification

**Table 7:** Identified piezoelectric tube's parameters

Parameter	Value	Units
Stiffness ( $\mathbf{K}$ )	27.5713	N/m
Damping ( $\mathbf{b}$ )	0.2821	Ns/m
Force factor	0.7557	V/N



## 6 Controller

To accomplish the objective of performing scanning tasks, a close-loop model should be designed. Figure 25 shows the block diagram to achieve the positioning control. The desired position  $\mathbf{p}^*$  of the robot's end enters to the a controller so as the position of the actuator  $\mathbf{p}_{PZT}$ , the boundary velocity of the actuator  $\mathbf{q}_{PZT}$  and the actual robot's end position  $\mathbf{p}$ . Two sensors measured the positions of the actuator and the rod. The output  $\beta(\mathbf{x})$  controls the required force of the actuator in order to have a boundary velocity at the base of the rod to move it to the desired positions. Finally, the force factor multiplied this output force in order to have the necessary voltage.

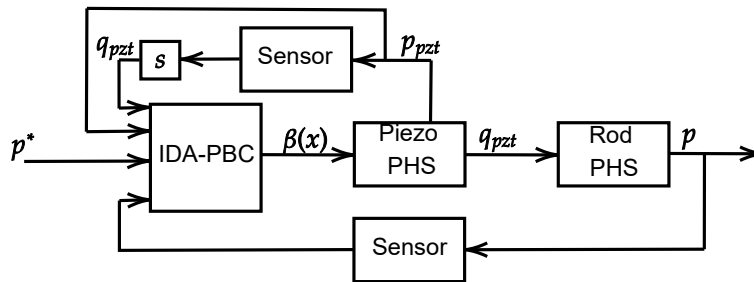


Figure 25: Block Diagram of the close-loop system

### 6.1 IDA-PBC Boundary Controller

The chosen control was a Interconnection Damping and Assignment-Passivity Based Controller (IDA-PBC). The main objective is to find a static state-feedback control  $u(x) = \beta(x)$  (equation (56)) such that the closed-loop dynamics is a PHS with interconnection and dissipation of the form  $\dot{x} = (J_d - R_d) \frac{\delta H_d}{\delta x}$ . In which  $J_d$  and  $R_d$  are desired matrices of interconnection and dissipation respectively.

$$\beta(\mathbf{x}) = (g^T g)^{-1} g^T \left[ (J_d - R_d) \frac{\delta H_d}{\delta x} - (J - R) \frac{\delta H}{\delta x} \right] \quad (56)$$

For the IDA-passivity based controller, the matching equation (57) should be satisfied. For this, a proper annihilator  $g^\perp$  should be selected such that  $g^\perp g = 0$ .

$$g^\perp \left[ (J_d - R_d) \frac{\delta H_d}{\delta x} - (J - R) \frac{\delta H}{\delta x} \right] = 0 \quad (57)$$

In equation (58) the desired Hamiltonian is shown, two new variables are presented in this equation,  $\tilde{\mathbf{K}}$  and  $\mathbf{p}^*$ , that represent a desired damping injection for the actuator and the desired position of the continuum robot respectively. The solved matching equation is shown in (59) by presenting the variable  $\tilde{\mathbf{b}}$  in the matrix  $R_d$  which represents a desired damping injection in the actuator.



$$\mathcal{H}_d = \frac{1}{2} \mathbf{K}_{se} (\mathbf{v} - \mathbf{v}^*)^2 + \frac{1}{2} \mathbf{q}^2 + \frac{1}{2} \mathbf{K}_{bt} (\mathbf{u} - \mathbf{u}^*)^2 + \frac{1}{2} \boldsymbol{\omega}^2 + \frac{1}{2} \tilde{\mathbf{K}} (\mathbf{p} - \mathbf{p}^*)^2 + \frac{1}{2} \mathbf{q}_{PZT}^2 \quad (58)$$

$$\underbrace{\begin{bmatrix} I_n & 0 & 0 & 0 & 0 & 0 \\ 0 & I_n & 0 & 0 & 0 & 0 \\ 0 & 0 & I_n & 0 & 0 & 0 \\ 0 & 0 & 0 & I_n & 0 & 0 \\ 0 & 0 & 0 & 0 & I_n & 0 \end{bmatrix}}_{g^\perp} \left[ \begin{array}{cccc|cc} 0 & D + \hat{\mathbf{u}} & 0 & \hat{\mathbf{v}} & 0 & g_1 \\ -D^T + \hat{\mathbf{u}} & -\rho A \hat{\boldsymbol{\omega}} - \mathbf{B}_{se} & 0 & 0 & 0 & 0 \\ 0 & 0 & 0 & D + \hat{\mathbf{u}} & 0 & 0 \\ \hat{\mathbf{v}} & 0 & -D^T + \hat{\mathbf{u}} & -\rho \mathbf{J} \boldsymbol{\omega} - \mathbf{B}_{bt} & 0 & 0 \\ \hline 0 & 0 & 0 & 0 & 0 & 1 \\ -g_1^T & 0 & 0 & 0 & -1 & -\tilde{\mathbf{b}} \end{array} \right] \begin{bmatrix} \mathbf{K}_{se} (\mathbf{v} - \mathbf{v}^*) \\ \mathbf{q} \\ \mathbf{K}_{bt} (\mathbf{u} - \mathbf{u}^*) \\ \boldsymbol{\omega} \\ \tilde{\mathbf{K}} (\mathbf{p} - \mathbf{p}^*) \\ \mathbf{q}_{PZT} \end{bmatrix} \begin{array}{l} \\ \\ \\ \\ \frac{\delta \mathcal{H}_d}{\delta \mathbf{x}} \end{array} \quad (59)$$

$$- \left[ \begin{array}{cccc|cc} 0 & D + \hat{\mathbf{u}} & 0 & \hat{\mathbf{v}} & 0 & g_1 \\ -D^T + \hat{\mathbf{u}} & -\rho A \hat{\boldsymbol{\omega}} - \mathbf{B}_{se} & 0 & 0 & 0 & 0 \\ 0 & 0 & 0 & D + \hat{\mathbf{u}} & 0 & 0 \\ \hat{\mathbf{v}} & 0 & -D^T + \hat{\mathbf{u}} & -\rho \mathbf{J} \boldsymbol{\omega} - \mathbf{B}_{bt} & 0 & 0 \\ \hline 0 & 0 & 0 & 0 & 0 & 1 \\ -g_1 & 0 & 0 & 0 & -1 & -\mathbf{b} \end{array} \right] \begin{bmatrix} \mathbf{K}_{se} (\mathbf{v} - \mathbf{v}^*) \\ \mathbf{q} \\ \mathbf{K}_{bt} (\mathbf{u} - \mathbf{u}^*) \\ \boldsymbol{\omega} \\ \mathbf{K} \mathbf{p}_{PZT} \\ \mathbf{q}_{PZT} \end{bmatrix} \begin{array}{l} \\ \\ \\ \\ \frac{\delta \mathcal{H}}{\delta \mathbf{x}} \end{array}$$

$$= \begin{bmatrix} I_n & 0 & 0 & 0 & 0 & 0 \\ 0 & I_n & 0 & 0 & 0 & 0 \\ 0 & 0 & I_n & 0 & 0 & 0 \\ 0 & 0 & 0 & I_n & 0 & 0 \\ 0 & 0 & 0 & 0 & I_n & 0 \end{bmatrix} \begin{bmatrix} 0 \\ 0 \\ 0 \\ 0 \\ 0 \\ -\tilde{\mathbf{K}} (\mathbf{p} - \mathbf{p}^*) - \tilde{\mathbf{b}} \mathbf{q}_{PZT} + \mathbf{K} \mathbf{p}_{PZT} + \mathbf{b} \mathbf{q}_{PZT} \end{bmatrix} = \begin{bmatrix} 0 \\ 0 \\ 0 \\ 0 \\ 0 \\ 0 \end{bmatrix}$$

The controller variable in equation (56) is solved as in equation (60) giving a final control law shown in equation (61).

$$\boldsymbol{\beta}(\mathbf{x}) = [0 \ 0 \ 0 \ 0 \ 0 \ 1] \begin{bmatrix} 0 \\ 0 \\ 0 \\ 0 \\ 0 \\ -\tilde{\mathbf{K}} (\mathbf{p} - \mathbf{p}^*) - \tilde{\mathbf{b}} \mathbf{q}_{PZT} + \mathbf{K} \mathbf{p}_{PZT} + \mathbf{b} \mathbf{q}_{PZT} \end{bmatrix} \quad (60)$$

$$\boldsymbol{\beta}(\mathbf{x}) = \tilde{\mathbf{K}} (\mathbf{p}^* - \mathbf{p}) + \mathbf{K} \mathbf{p}_{PZT} + (\mathbf{b} - \tilde{\mathbf{b}}) \mathbf{q}_{PZT} \quad (61)$$

## 6.2 Simulation

For the controller simulation, the *Simulink* model shown in Figure 12 was changed as the one shown in Figure 26. In this model, the controller and the piezoelectric model are included. Also, the free end position of the robot and the velocity of the piezo tube are recovered. The velocity  $\mathbf{q}_{PZT}$  goes directly to the rod's model as the boundary condition  $\mathbf{e}_0^2$ . The variables  $\tilde{\mathbf{K}} = 50$  and  $\tilde{\mathbf{b}} = 1$  where chosen.

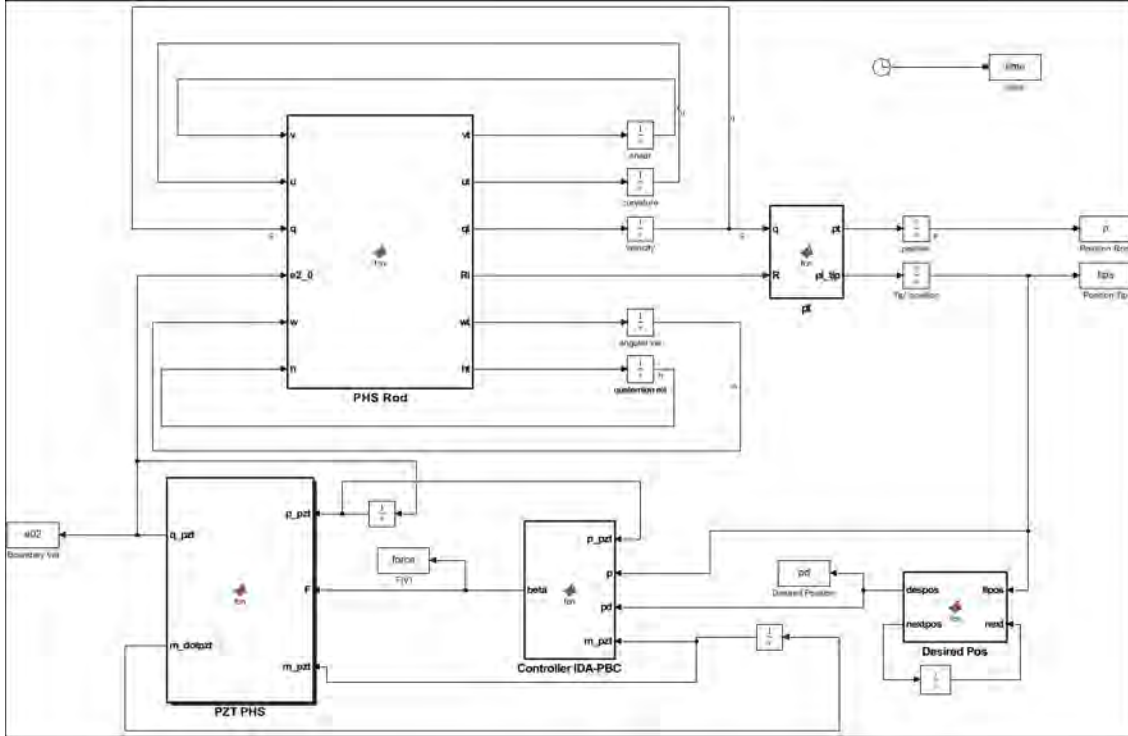


**Figure 26:** Simulink close-loop complete model

The first performed simulation consisted in given a desired position in both  $x$  and  $y$  directions. In this case, a desired position of  $20\mu\text{m}$  in  $x$  and  $-20\mu\text{m}$  in  $y$  was chosen. Figure 27 shows the response of the controller. In the two graphs above, the current position against the desired position is plotted. In the middle graph, the error between the desired position and the current position is shown.

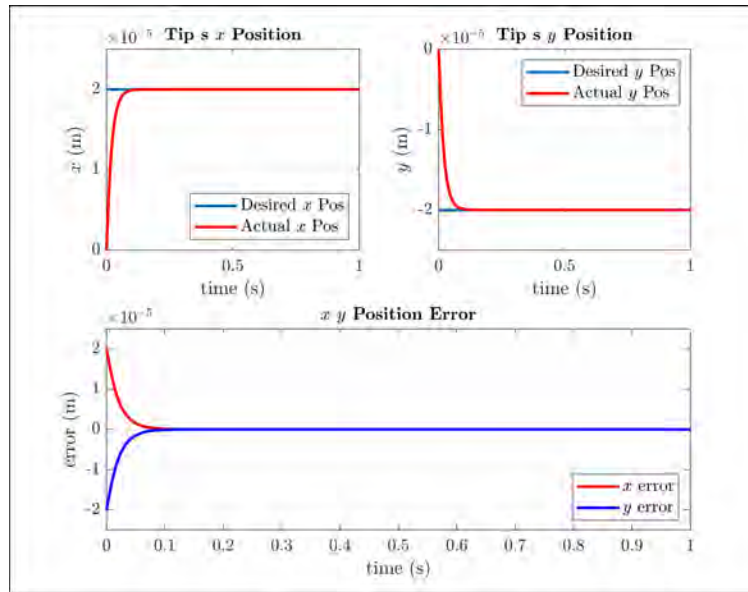


**Figure 27:** Simulation for a desired  $[x, y]$  position

The second numerical validation was to give a scanning trajectory in the form of a spiral. This trajectory consisted in giving a final position, in this case was the coordinate  $[0, 10\mu m]$ . Then, the trajectory was performed in 100 points and 3 turns. Figure 28 shows these 100 points and the trajectory that the robot followed. In Figure 29, the response of the controller is shown. In the two graphs above, the current position against the desired position is plotted. In the middle graph, the error between the desired position and the current position is shown. Finally, in the graph at the bottom, the velocity of the actuator is plotted.

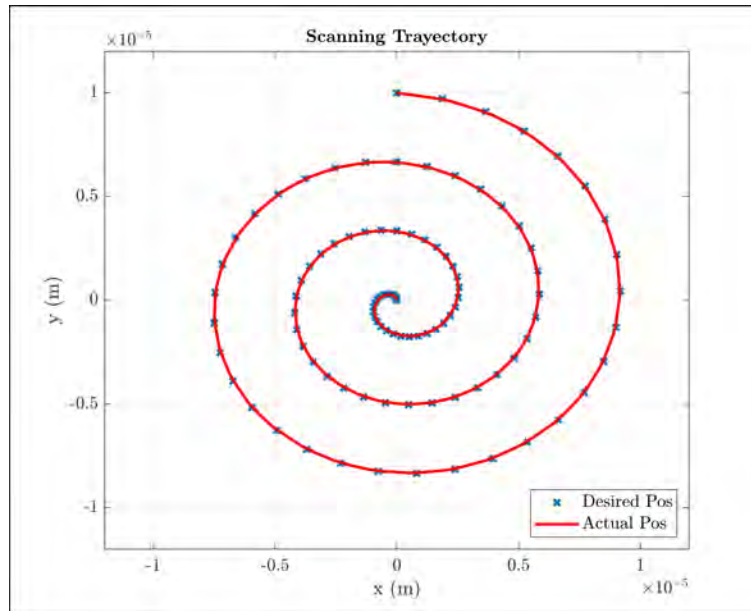


Figure 28: 100 points scanning spiral trajectory

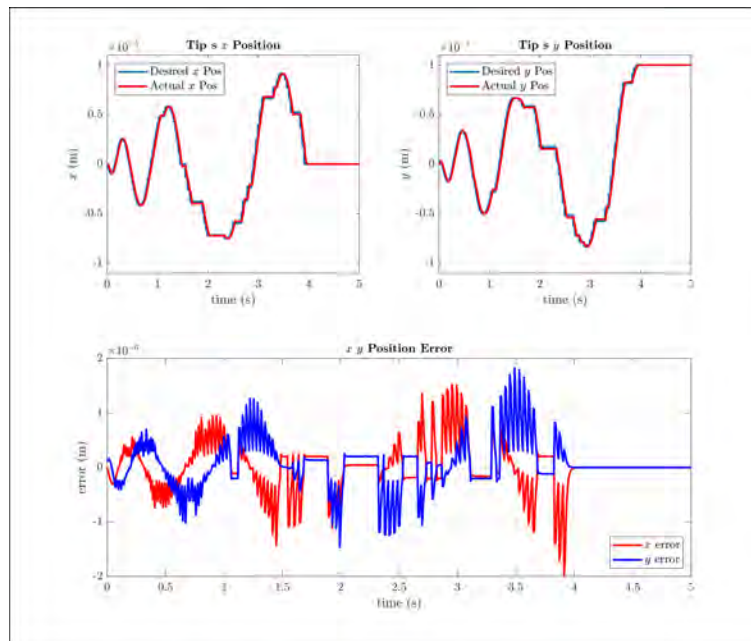


Figure 29: Simulation for a desired  $[x, y]$  trajectory

### 6.3 Experimental validation

The final part was to do an experimental validation of the controller: As mentioned before, this validation was just performed in 1D. The communication to the experimental setup was made with the *Simulink* program shown in Figure 30 in which the sensors data was recovered in two *analog to digital converter* ports and the voltage was sent to the amplifiers by one *digital to analog converter* port of the *CP1104* board. The interface and final communication was made in the dSpace program *Control Desk*. Figure 31 shows the designed interface in which  $\mathbf{p}^*$ ,  $\tilde{\mathbf{K}}$  and  $\tilde{\mathbf{b}}$  could be modified and  $\mathbf{p}_{PZT}$  and  $\mathbf{p}$  are plotted in real time. For the experimental validation, the parameters  $\tilde{\mathbf{K}} = 500$  and  $\tilde{\mathbf{b}} = 1$  where tuned.

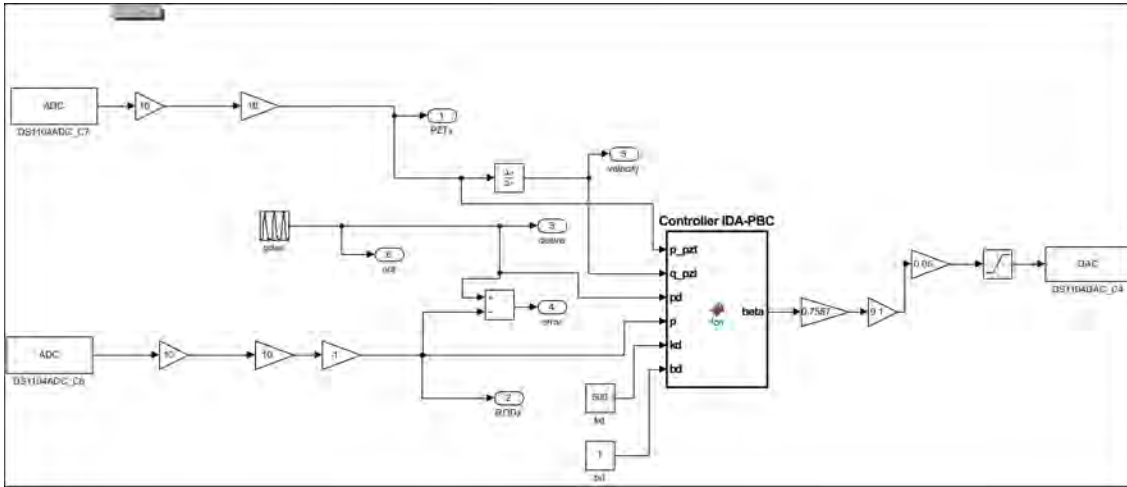


Figure 30: Simulink program for dSpace

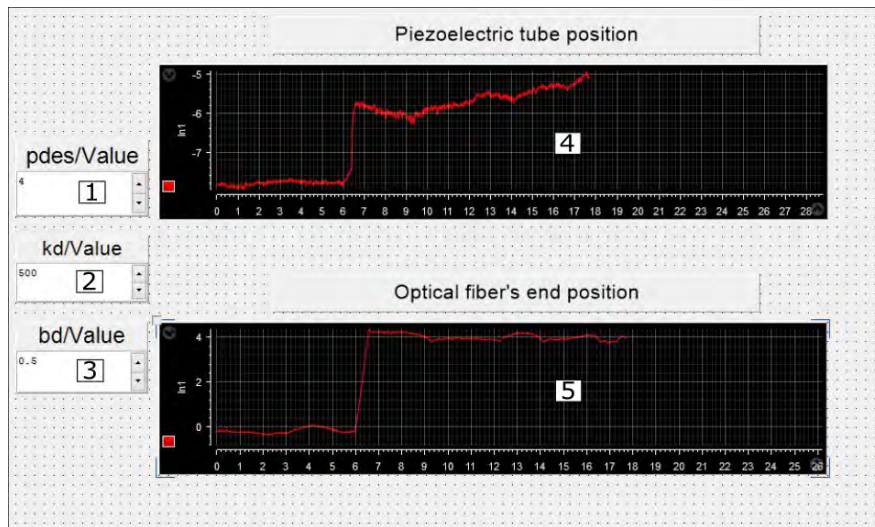
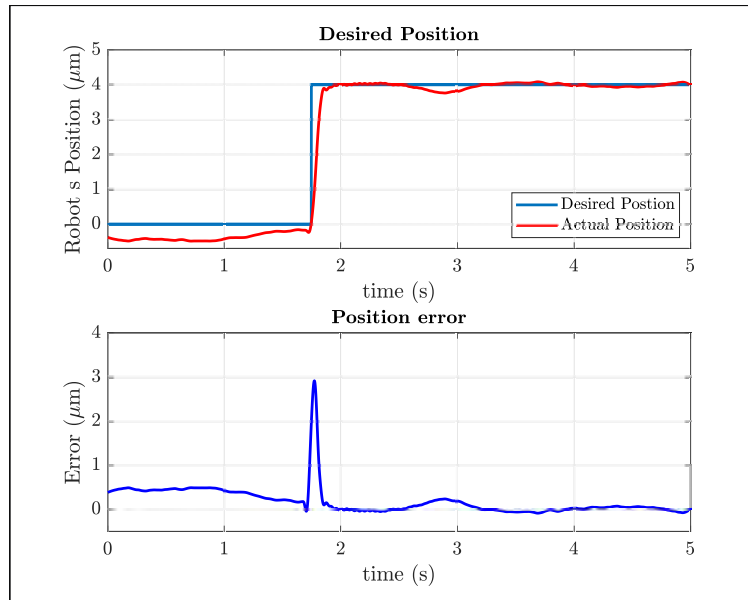


Figure 31: Control Desk interface. 1: Desired position  $\mathbf{p}^*$ ; 2: Desired energy shaping  $\tilde{\mathbf{K}}$ ; 3: Desired damping injection  $\tilde{\mathbf{b}}$ ; 4: Current actuator position  $\mathbf{p}_{PZT}$ ; 5: Current fiber position  $\mathbf{p}$

As in the simulation part, the first thing to validate was a desired position. For the results shown in Figure 32 a desired position of  $4\mu\text{m}$  was selected. The plot at the top shows the desired position against the actual position of the continuum robot's free end. The error of these two positions is plotted at the bottom. The obtained result is similar to the simulated one. The positioning is not 100% accurate due to several factors; noise in the measurements of the positions with the sensors, environmental perturbation and the non-linearities of the actuator that were not taken into account.



**Figure 32:** Experimental result for a desired position of  $4\mu\text{m}$

As an extra validation, Figure 33 also shows a response to a  $6\mu\text{m}$  desired position, but in this case, a rude perturbation was introduced on purpose to the system by touching the optical fiber to observe its stabilization. It can be observed from the graph at the top, that even the perturbation caused a movement to  $-21\mu\text{m}$  the controller achieved to return the robot to the commanded position.

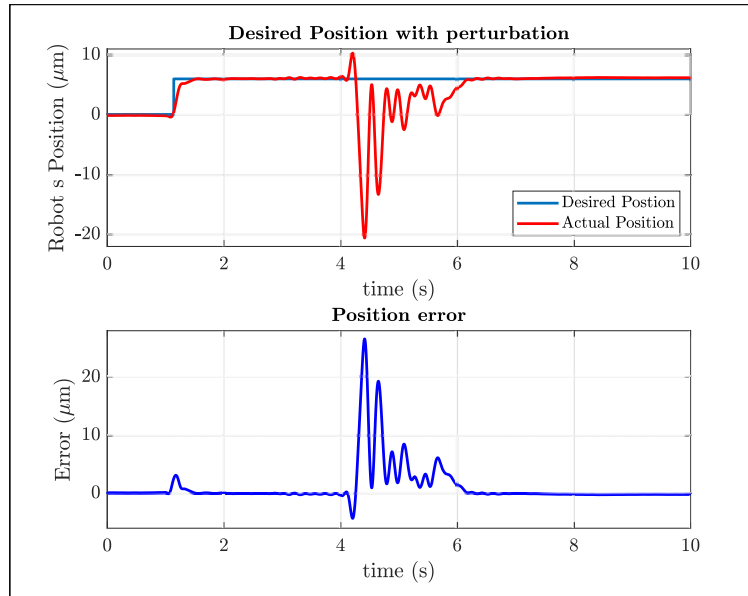


**Figure 33:** Experimental result for a desired position of  $6\mu m$  with a perturbation

The final validation was to command a desired time-changing trajectory and see the response of the continuum robot. The plotting at the top of Figure 34 shows the actual position trajectory against the desired trajectory. It could be appreciated from the plot in the middle that the error is between  $-0.5\mu m$  and  $0.5\mu m$ .

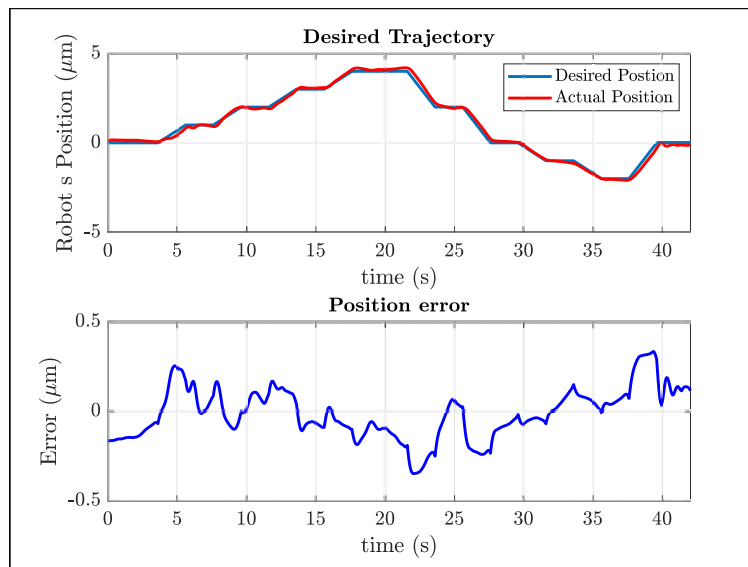


**Figure 34:** Experimental result for a desired trajectory

## 7 Conclusions and Perspectives

This internship project developed within the micro and nano robotics team at the AS2M department presents a port Hamiltonian approach for a piezoelectric tube actuated flexible optical fiber. The dynamics of the optical fiber were described by the Cosserat rod model under the port Hamiltonian framework approach. An IDA-passivity based control was developed to control the optical fiber's free end. Numerical simulations were done to validate both, the new proposed model and the controller. The simulations for validating the PHS model were done by applying a force at the the rod's end as if the tip was pulled, then the force was released and the behavior was observed. The Cosserat and the PHS model were compared with this same method. The controller simulation was performed in the  $[x, y]$  directions by commanding a desired position and a desired trajectory. At last, an experimental validation was also performed. In this validations, some physical parameters were identified for the optical fiber and for the piezoelectric tube actuator. The controller was then validated in just the  $x$  direction. The obtained results in the experimental part were quite acceptable even the problems caused by environmental perturbations.

This current work involved and put together several disciplines. For example, the complete CAD for the supports and its printing in 3D printing machines. It also included the training for the usage of the MEMS analyzer, and the port Hamiltonian systems theory, which are defined by the power preserving property by the geometric notion of a Dirac structure.

The work also presented some difficulties, for example, the simulations done for the PHS were too heavy and slow to perform due to the discretization and the stiffness of the model. Also the measurement of the free end of the optical fiber was planned to be done with a PSD (position-sensitive detector). A laser spot emitted by the fiber was supposed to hit the sensor and with the recovered voltages the  $[x, y]$  position was supposed to be obtained. The problem with this sensor was that the laser emitted from the fiber was not collimated (a divergent ray was emitted), so the sensor was not able to capture in a proper way the light. The lack of proper equipment to measure the position causes that the experimental validation was done only in the  $x$  direction.

For future work measurements of the position in both  $[x, y]$  directions need to be investigated. Also for better results, more parameters of the rod should be included into the controller, this could be done by adding a non-linear observer to estimate these parameters that can not be measured. And also, the non-linearities of the actuator, such as hysteresis and creep, could be compensated.



## Bibliography

- [1] Jessica Burgner-Kahrs D. Caleb Rucker and Howie Choset. Continuum robots for medical applications: a survey. *IEEE TRANSACTIONS ON ROBOTICS*, 31:1261–1280, 2015.
- [2] John Till and D. Caleb Rucker. Elastic rod dynamics: Validation of a real-time implicit approach. *IEEE/RSJ International Conference on Intelligent Robots and Systems (IROS)*, 2017.
- [3] John Till Vincent Aloï and Caleb Rucker. Real-time dynamics of soft and continuum robots based on Cosserat rod models. *The International Journal of Robotics Research*, 38(6):723–746, 2019.
- [4] Arjan van der Schaft. Port-Hamiltonian modeling for control. *Annual Review of Control, Robotics, and Autonomous Systems*, 2020.
- [5] D. Caleb Rucker and Robert J. Webster III. Statics and dynamics of continuum robots with general tendon routing and external loading. *IEEE TRANSACTIONS ON ROBOTICS*, 27(6):1033–1044, 2011.
- [6] Heng-Sheng Chang Udit Halder Chia-Hsien Shih Arman Tekinalp Tejaswin Parthasarathy Ekaterina Gribkova Girish Chowdhary Rhanor Gillette Mattia Gazzola Prashant G. Mehta. Energy shaping control of a cyberoctopus soft arm. 2004.
- [7] Alessandro Macchelli and Claudio Melchiorri. Modeling and control of the timoshenko beam: the distributed port Hamiltonian approach. *SIAM J. CONTROL OPTIM*, 43(2):743–767, 2004.
- [8] John Daniel Till. *On the Statics, Dynamics, and Stability of Continuum Robots: Model Formulations and Efficient Computational Schemes*. 2019.
- [9] Y. Le Gorrec H. Zwart and B. Maschke. Dirac structures and boundary control systems associated with skew-symmetric differential operators. *SIAM J. Control Optimization*, 44(5):1864–1892, 2005.
- [10] Vincent Trenchant Hector Ramirez Yann Le Gorrec Paul Kotyczka. Structure preserving spatial discretization of 2D hyperbolic systems using staggered grids finite difference. *American Control Conference*, 2017.
- [11] Vincent Trenchant Hector Ramirez Yann Le Gorrec Paul Kotyczka. Finite differences on staggered grids preserving the port-Hamiltonian structure with application to an acoustic duct. *Journal of Computational Physics*, 2018.
- [12] Ning Liu. *Port-Hamiltonian modeling and distributed control of flexible structures: application to bio-medical endoscopes with electro-active polymer actuators*. 2020.